ARTICLES
https://doi.org/10.1038/s41565-022-01125-0

nature nanotechnology

A pyroptosis nanotuner for cancer therapy

Binlong Chen[1,2], Yue Yan[2], Ye Yang[2], Guang Cao[2], Xiao Wang[3], Yaoqi Wang[2], Fangjie Wan[2], Qingqing Yin[2], Zenghui Wang[2], Yunfei Li[3], Letong Wang[2], Bo Xu[1], Fuping You[3] ✉, Qiang Zhang[1,2] ✉ and Yiguang Wang[1,2] ✉

Pyroptosis is a gasdermin-mediated programmed necrosis that occurs via membrane perforation and that can be exploited for biomedical applications in cancer therapy. However, inducing specific pyroptotic cancer cell death while sparing normal cells is challenging. Here, we report an acid-activatable nanophotosensitizer library that can be used to spatiotemporally target distinct stages of endosomal maturation, enabling tunable cellular pyroptosis. Specific activation of phospholipase C signalling transduction in early endosomes triggers gasdermin-E-mediated pyroptosis, which is dramatically reduced when acid-activatable nanophotosensitizers are transported into late endosomes/lysosomes. This nanotuner platform induces pyroptotic cell death with up to 40-fold tunability in various gasdermin-E-positive human cancers, resulting in enhanced anti-tumour efficacy and minimized systemic side effects. This study offers new insights into how to engineer nanomedicines with tunable pyroptosis activity through specific targeting of distinct endocytic signalling for biomedical applications.

Pyroptosis is a newly defined mode of programmed cell death with the characteristics of rapid membrane rupture, cell swelling with large bubbles and release of cellular proinflammatory contents[1]. Pyroptosis plays vital pathophysiological roles in pathogen infections, atherosclerosis, diabetics and organ failures that are triggered by the inflammatory caspase-mediated gasdermin D (GSDMD) cleavage[2,3]. Recently, gasdermin E (GSDME) was identified as the substrate of caspase-3 that executes pyroptotic cancer cell death and also induces the systemic side effects of chemotherapy drugs[4,5]. In addition, the cleavage of gasdermins triggers the inflammatory tumour microenvironment and enhances the efficacy of cancer immunotherapy[6,7]. Accumulating evidence shows that pyroptosis can be induced by endocytic organelle stress. A variety of inorganic nanoparticles, including metal oxide nanoparticles[8], carbon black nanoparticles[9], mesoporous silica nanoparticles[10] and metal–organic framework nanoparticles[11], induce pyroptosis in different cell types in an uncontrolled manner. The pyroptotic cell death elicited by these nanoparticles represents potential biomedical applications and biosafety concerns. In cancer therapy, there is an urgent need to develop a powerful nanotechnology to achieve pyroptotic killing specific to cancers rather than normal tissues.

Endosomes and lysosomes play critical roles in physiological functions such as cell proliferation, protein/lipid catabolism, cell death and immune response[12]. Upon endocytosis, receptors are translocated from plasma membranes to endocytic organelle membranes, and the resulting compartment system serves as an essential station for signalling transduction. For therapeutic applications, specific delivery of payloads from nanoparticles to their intracellular targets within certain endocytic regions is important for achieving optimal therapeutic outcomes. Attention has been paid to the design of nanoparticles to target lysosomes and induce different modes of programmed cell death, such as caspase-independent lysosomal cell death[13], ferroptosis[14], autophagy[15] and pyroptosis[16]. However, it remains unknown whether the whole endosome/lysosome maturation stage participates in the signalling pathway of programmed cell death and how to regulate the pyroptosis-inducing activity of nanomaterials.

Herein, we engineered a small acid-activatable nanophotosensitizer (ANPS) library with a distinct pH transition (pH_t) from 6.9 to 5.3, covering the entire pH range of endosome maturation stages ($pH = 7.0–5.0$). Using this ANPS platform, we successfully divided the entire endosome maturation pathway into ten endocytic regions (pH interval, 0.2) and systemically investigated their ability to finely tune the pyroptosis-inducing activity in cancer cells via precise targeting of each acidic endocytic region in vitro and in vivo (Fig. 1). The underlying mechanism of fine-tuned pyroptotic cell death by these nanomaterials was also uncovered. We found that the ANPS could specifically elicit GSDME-mediated pyroptosis in various GSDME-positive cancer cells through specific activation of phospholipase C (PLC), signalling transduction by lipid peroxidation, a process initiated by nanophotosensitizer-mediated oxidative stress in early endosomes; however, its pyroptosis-inducing activity was dramatically diminished after nanocargo transportation into late endosomes and lysosomes. Therefore, this pyroptosis nanotuner achieved striking therapeutic efficacy on various human GSDME-expressing cancer types accompanied with minimized systemic side effects in vivo. The study offers new insights into how endosome maturation precisely tunes the pyroptosis-inducing activity of nanomaterials and provides a basis for pyroptosis-mediated cancer immunotherapy.

Design of ANPS library for distinct killing of cancer cells

Based on our developed ultra-pH-sensitive nanotechnology[17–19], we synthesized a series of amphiphilic copolymers mPEG-b-P(R_1-r-R_2), where poly(ethylene glycol) methyl ether (mPEG) serves as a hydrophilic block and P(R_1-r-R_2) is an ionizable hydrophobic block (Supplementary Fig. 1 and Supplementary Table 1). The pK_a of these block copolymers ranged from 5.2 to 6.8 with pH increments of 0.2 as determined by titration methods. The photosensitizer (chlorin e6, Ce6) and fluorescence quencher (QSY21) were conjugated

---

[1]State Key Laboratory of Natural and Biomimetic Drugs, School of Pharmaceutical Sciences, Peking University, Beijing, China. [2]Beijing Key Laboratory of Molecular Pharmaceutics and New Drug Delivery System, School of Pharmaceutical Sciences, Peking University, Beijing, China. [3]Institute of Systems Biomedicine, Department of Immunology, Beijing Key Laboratory of Tumour Systems Biology, Peking University Health Science Center, Beijing, China.
✉e-mail: fupingyou@hsc.pku.edu.cn; zqdodo@bjmu.edu.cn; yiguang.wang@pku.edu.cn

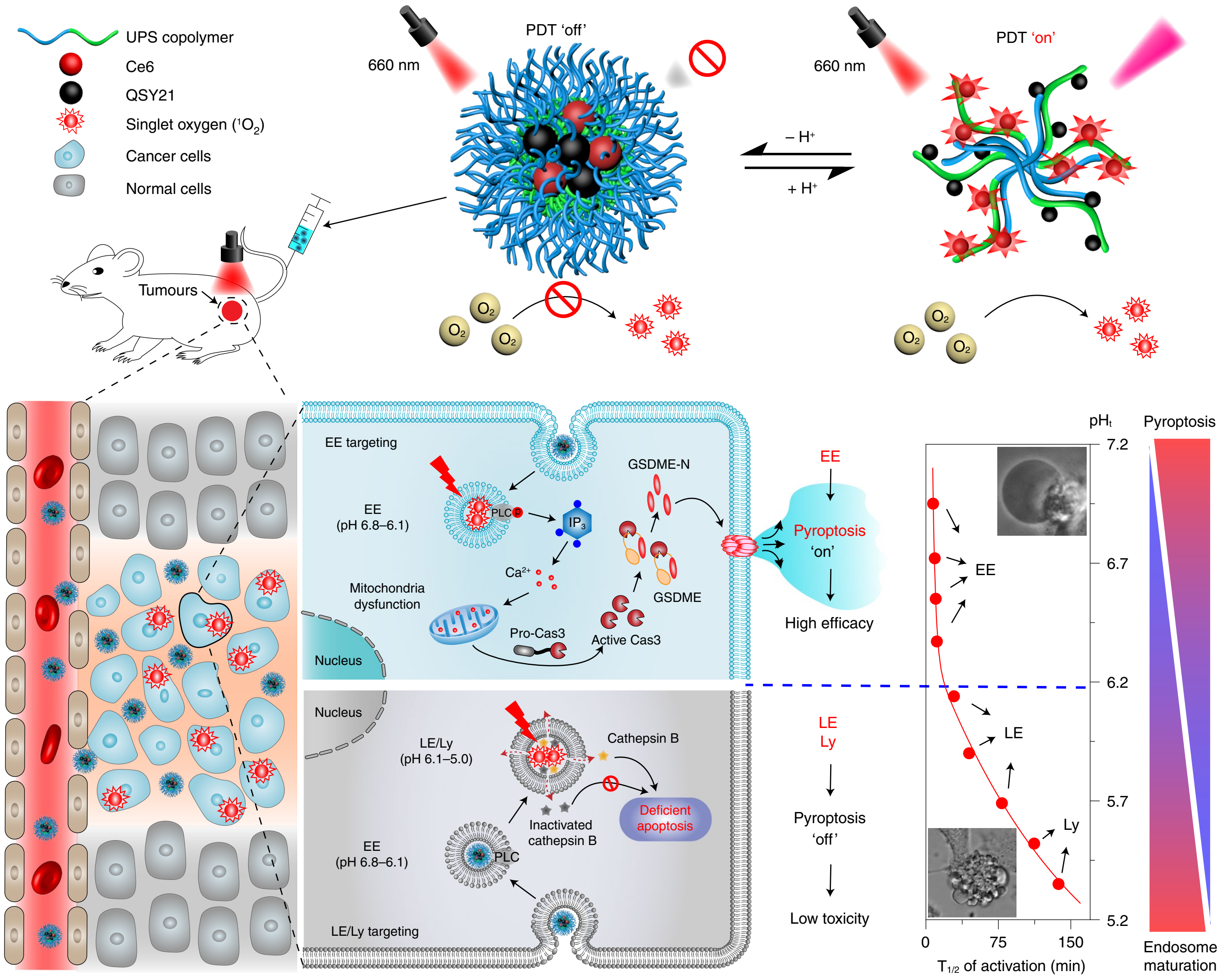

Fig. 1 | Schematic illustrations of ANPS and the tunable pyroptosis evoked by the ANPS library through temporal differentiation of endosome maturation. The ANPS kept the PDT silent during blood circulation and extracellular distribution. Upon endocytosis, the ANPS library with tunable pH_t was specifically activated along the pH gradients (pH 5.0–7.0) during the endosome maturation pathway. In cancer cells, after activation in EE, the ANPS induced robust pyroptotic cell death via caspase-3 (Cas3)-mediated GSDME cleavage. By sharp contrast, the pyroptosis-inducing activity of ANPS was diminished after maturation into LE and Ly, due to the photo-inactivation of cathepsin B and deficient caspase-3 activation. This tunable pyroptosis results from the differential targeting of distinct maturation stages, rising from the activation of PLC (phospholipase C) by lipid peroxidation in EE, followed by the caspase-3-mediated cleavage of GSDME and ending with extensive GSDME-induced pyroptotic cell death. The absence of PLC and inactivation of cathepsin B in LE and Ly cause deficient apoptosis, leading to the low toxicity to normal tissues after relatively long drug-light intervals. UPS, ultra pH sensitive; P, phosphorylation; $T_{1/2}$, half time.

to the copolymers with high conjugation efficiency. Then, a small ANPS library containing nine nanoparticles was successfully engineered, with each nanoparticle comprising an equal fraction of QSY21-conjugated copolymer and Ce6-conjugated copolymer. All the ANPS exhibited 200-fold fluorescence and 300-fold singlet oxygen generation (SOG) amplification with excellent synchronism and sharp response (Fig. 2a,b and Supplementary Table 2). Each ANPS from the library stayed 'off' at pH 7.4, while it disassembled and triggered the photodynamic therapy (PDT) to 'on' at the predesigned pH_t from 5.3 to 6.9 (Fig. 2c and Supplementary Figs. 2–4).

To verify whether the ANPS library could distinguish the tiny pH difference among endocytic compartments during endosome maturation, we investigated the subcellular localization and activation kinetics of the ANPS in A549 cells by the pulse–chase method (Fig. 2d). Confocal images indicated that a punctate $ANPS_{6.9}$ (ANPS with pH_t of 6.9) signal appeared immediately after endocytosis in the early endosomes (EE, RAB5A-positive). By contrast, $ANPS_{6.1}$ and $ANPS_{5.3}$ kept silent during the early stage of endocytosis and then illuminated after endosome maturation for 1 h into late endosomes (LE, RAB7A-positive) or 2 h into lysosomes (Ly; lysosomal-associated membrane protein 1 (LAMP1)-positive), respectively (Fig. 2e and Supplementary Figs. 5–8). The activation kinetics were also monitored with flow cytometry (Fig. 2f). The half-lives of cellular activation for the ANPS with distinct pH_t (from 6.9 to 5.3) gradually increased from 7.5 to 127 min, permitting the temporal differentiation of the entire endosome maturation pathway into ten endocytic regions (Fig. 2g). The real-time subcellular distributions of ANPS in EE, LE and Ly were further analysed (Supplementary Fig. 8d). The peak time for the percentage of ANPS in EE, LE and Ly is about 30, 60 and 180 min, respectively.

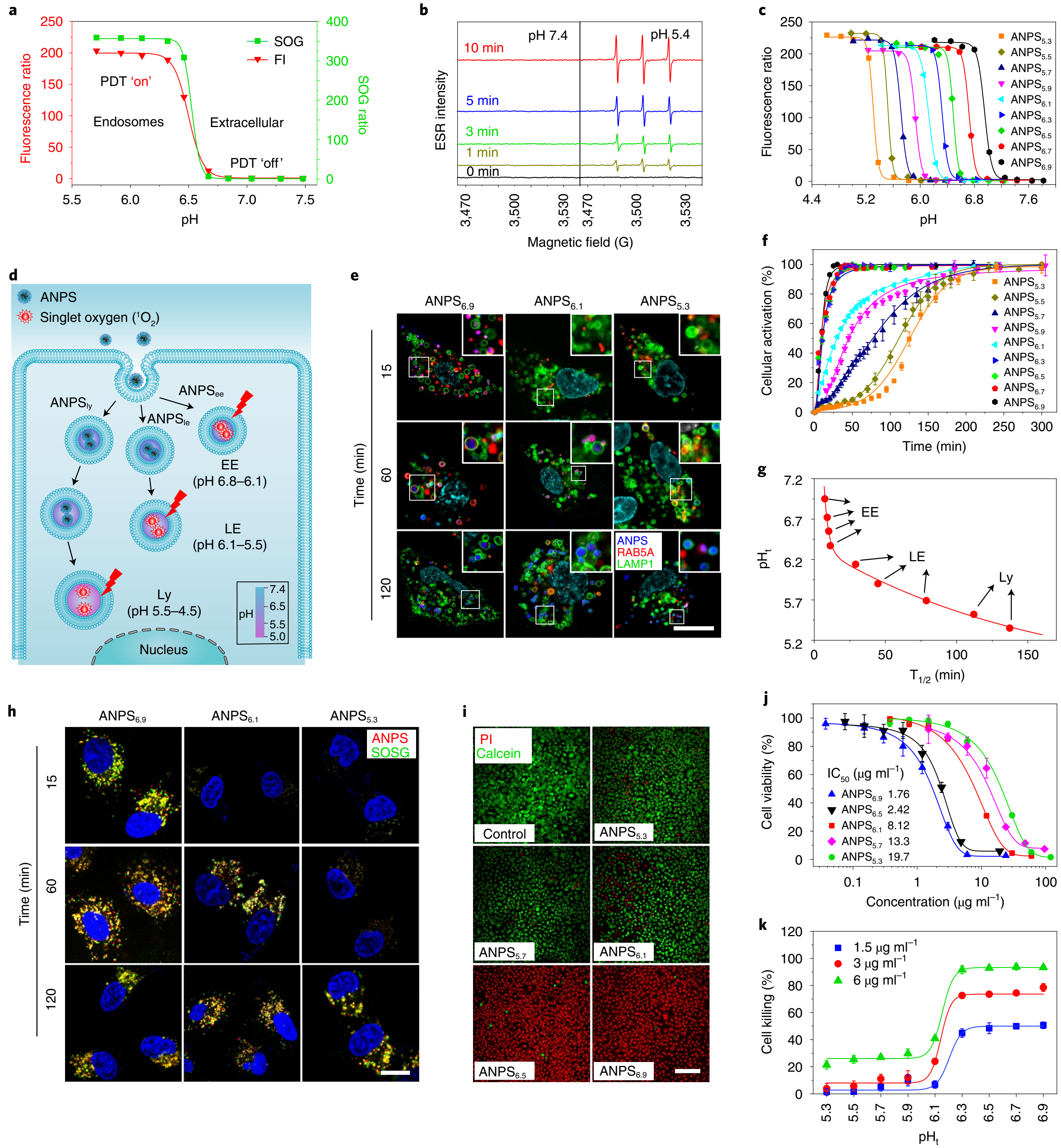

Fig. 2 | Tuning the organelle-specific cytotoxicity by engineering the ANPS library with pH differentiation capacity. **a**, Synchronous pH-dependent fluorescence intensity (FI) and SOG amplification behaviour of representative ANPS ($ANPS_{6.5}$) with high on/off ratio. **b**, Electron spin resonance (ESR) spectra of $ANPS_{6.5}$ in pH 7.4 and pH 5.4 (D_2O solution) when irradiated with a 660 nm laser (100 mW cm^{-2}) for 0–10 min. **c**, Fluorescence on/off ratio of ANPS library with a pH increment of 0.2, covering the intracellular range of pH 5.3–6.9 in a tumour microenvironment. **d**, A schematic of sequential activation of the ANPS library intracellularly to achieve specific endocytic organelle-targeted oxidative stress. **e**, Sequential cellular activation and endocytic organelle colocalization of the ANPS library. EE and Ly were transfected with RAB5A-RFP (RFP, red fluorescent protein) and LAMP1-GFP (GFP, green fluorescent protein), respectively. Scale bar = 10 μm. **f**, Cellular activation kinetics of ANPS library monitored with flow cytometry. Data are presented as mean ± s.d. (*n* = 3 independent experiments per group). **g**, The time for 50% activation of the ANPS library, calculated from **f**. **h**, Representative confocal images of intracellular SOG (green) and colocalization with ANPS (red) at predesignated time points. Scale bar = 10 μm. SOSG, singlet oxygen sensor green. **i**, Representative calcein/PI staining of A549 cells. Scale bar = 100 μm. **j**, Cell viability curves of ANPS-library-mediated oxidative stress against A549 cells measured by MTT assay. Data are presented as mean ± s.d. (*n* = 3 biologically independent experiments per group). **k**, Cell killing efficacy as a function of pH_t for the ANPS library measured by MTT assay. Data are presented as mean ± s.d. (*n* = 3 biologically independent experiments per group).

Moreover, we verified that the cellular SOG was coincident with the activation profile of ANPS (Fig. 2h and Supplementary Fig. 9) with high fidelity due to the extremely short lifespan (~0.03–0.18 ms) and limited active radius (~0.01–0.02 µm) of singlet oxygen[20]. These results demonstrated that the ANPS library can spatiotemporally differentiate each stage of endosome maturation into very subtle regions, permitting precisely endocytic organelle-targeted oxidative stress.

To examine whether the distinct endocytic organelle targeting of ANPS could influence the photocytotoxicity, we next evaluated the photo-killing of cancer cells by ANPS in vitro. Intriguingly, we found that the cell killing efficacy of $ANPS_{6.9}$ and $ANPS_{6.5}$ on A549 cells was dramatically stronger than that of $ANPS_{6.1}$, $ANPS_{5.7}$ and $ANPS_{5.3}$ with the same irradiation dose (Fig. 2i). The half-maximum inhibitory concentration (IC_{50}) values of $ANPS_{6.1}$ and $ANPS_{5.3}$ were 4.6-fold and 11.8-fold higher, respectively, than that of $ANPS_{6.9}$ (Fig. 2j). The differences in the photo-killing effect among the representative five ANPSs was further confirmed by staining with Annexin V fluorescein isothiocyanate (Annexin V-FITC) and propidium iodide (PI; Supplementary Fig. 10a). Moreover, the differences were ubiquitous on MCF-7 and HeLa cells (Supplementary Fig. 10b,c). We can divide the small library of nine ANPSs into two groups according to the photocytotoxicity efficacy, that is, EE-targeted and LE-/Ly-targeted ANPSs. The EE-targeted $ANPS_{6.9–6.3}$ exhibited dramatically higher photocytotoxicity than the LE-/Ly-targeted $ANPS_{6.1–5.3}$ (Fig. 2k).

Endosome maturation controls ANPS-induced pyroptosis

Previous studies have revealed that the varied chemical structures of ultra-pH-sensitive nanoprobes exhibited diverse functions in cellular metabolism modulation[21] and stimulator of interferon genes (STING) activation[22]. To exclude the chemical cues, we next investigated the photo-killing potency of the same ANPS in distinct endocytic organelles during endosome maturation (Fig. 3a). First we ruled out the impact of pH and endosome maturation on SOG ability upon ANPS activation (Supplementary Fig. 11). We unambiguously observed that ANPS manifested striking photocytotoxicity in the early stage of endosome maturation. Over 94% of A549 cells were killed when irradiated immediately after a 15 min pulse with $ANPS_{6.3–6.9}$ (0 h), and then the potency gradually weakened along with endosome maturation, even with the 1.5-fold-higher SOG in lysosome than in early endosome (Fig. 3b and Supplementary Figs. 11d and 12a,b). These huge differences were succinctly defined with the tunability index, the ratio of cell viability between any maturation time and 0 h. Results showed that the four EE-target ANPSs ($pH_t = 6.3–6.9$) rendered an up to 20-fold photo-killing tunability between the EE and Ly stages. However, the LE-/Ly-targeted ANPSs performed with negligible tunability between different endocytic organelles (Fig. 3b,c). The trend was further corroborated with the linear correlation ($R = 0.979$) between the percentage of ANPS in EE and the cell killing efficacy (Fig. 3d). Importantly, the tunable photocytotoxicity of ANPS was also generalized to other cell types including MCF-7 and HeLa cells (Fig. 3e). Considering that PDT dose governs cell death mechanism[23], we compared the cytotoxicity of PDT_{ee} (ANPS locates in EE) and PDT_{ly} (ANPS locates in Ly) at different Ce6 concentrations and laser powers. Obviously, the PDT_{ee} of $ANPS_{6.5}$ exhibited significantly stronger cell killing than the PDT_{ly} did, at various PDT doses (Supplementary Fig. 12c,d). The cell membrane is a vulnerable compartment, and its integrity can be directly destroyed by PDT[23]. To exclude the direct photodamage of ANPS at the cell membrane, we established an 'Always-On' nanophotosensitizer that presented the same fluorescence and SOG before and after endocytosis (Supplementary Fig. 2d,e). As expected, the Always-On nanophotosensitizer exhibited non-selective cytotoxicity at the cell membrane and in early endosomes, whereas $ANPS_{6.5}$ kept silent with undetectable cytotoxicity when binding to the cell membrane, followed by specific activation and dramatically increased photo-killing in early endosomes (Supplementary Fig. 13a–d). Moreover, the differences in PDT efficacy along the endosome maturation process were not achieved by free Ce6 due to its uncontrolled intracellular distribution (Supplementary Fig. 13e,f). The endosome maturation-tunable photocytotoxicity was further demonstrated in five tumour and three normal cell lines. Similarly, $ANPS_{6.5}$ exhibited significantly stronger photocytotoxicity by PDT_{ee} on both tumour cells and normal cells, with the tunability index varying from 3.2 to 42.5 (Fig. 3f and Supplementary Figs. 14 and 15). Therefore, we demonstrated that the ANPS-mediated photo-killing capacity can be modulated through temporal targeting of distinct endosome/lysosome maturation stages.

Importantly, we noted that the dying cells triggered by PDT_{ee} showed evident cell swelling and giant bubbles from the plasma membrane along with quickly enhanced permeability indicated by PI staining (Fig. 3g,h and Supplementary Video 1), which are typical characteristics of pyroptosis[1,2], whereas PDT_{ly} induced marginal alterations in cell viability and membrane permeability with the same PDT dose (Supplementary Figs. 14 and 15 and Supplementary Video 2). To confirm the nature of PDT-induced cell death, staining with Annexin V and PI, and lactate dehydrogenase (LDH), ATP and HMGB1 release analyses (Fig. 3i–l and Supplementary Figs. 16 and 17) were performed. These results demonstrated that robust pyroptosis was induced by the PDT_{ee} strategy.

PDT in EE evokes GSDME-mediated pyroptosis

We next elucidated the mechanism of tunable pyroptosis evoked by ANPS-mediated PDT. GSDMD and GSDME are two comprehensively investigated executors of pyroptosis[3]. The immunoblots of time-dependent gasdermin cleavage revealed that PDT_{ee} induced increasing GSDME-N fragments within a 6 h post-irradiation period in four tumour cell types (Supplementary Fig. 18), while no detectable cleaved GSDMD fragment was observed (Supplementary Fig. 19). The ANPS-library-mediated GSDME cleavage (Fig. 4a) and maturation-time-dependent GSDME cleavage (Fig. 4b) further revealed that the EE-targeted ANPS achieved a tunable pyroptosis activity through endosome maturation. More importantly, PDT_{ee} triggered robust GSDME cleavage compared to PDT_{ly}, with the same PDT dose at different tumour cell types (Fig. 4c). Genetic knockout studies further confirmed that $GSDME^{-/-}$ successfully avoided cell death induced by PDT_{ee}, converting pyroptosis to apoptosis. By contrast, $GSDMD^{-/-}$ cells still underwent pyroptosis with unchanged PDT efficacy (Fig. 4d,e, Supplementary Fig. 20 and Supplementary Videos 3 and 4). Furthermore, in vivo studies demonstrated that the anti-tumour efficacy of ANPS-mediated PDT_{ee} was dramatically suppressed on $GSDME^{-/-}$ A549 and MCF-7 tumour models (Fig. 4f and Supplementary Figs. 21 and 22). We also revealed that the GSDME expression in 14 human tumour cells exhibited a positive correlation with PDT_{ee} efficacy (Fig. 4g and Supplementary Fig. 23). Among these 14 cells, 12 cancer cells expressed GSDME at a level no less than that in SKOV3 and presented robust PDT_{ee} cell killing. Intriguingly, upregulating the expression of GSDME in SKOV3 cells with the DNA methyltransferase inhibitor decitabine[4] further boosted its sensitivity to PDT_{ee} (Supplementary Fig. 24). Inhibitor assays and immunoblotting results ruled out necroptosis[24] and ferroptosis[14] as being involved in $ANPS_{6.5}$-mediated PDT_{ee} (Supplementary Fig. 25).

Caspase-3 is the upstream pathway of GSDME-mediated pyroptosis[4,5]. Results showed that PDT_{ee} induced rapid and 10.9-fold activation of caspase-3 as compared to PDT_{ly}. GSDME knockout considerably diminished the kinetics and magnitude of caspase-3 activation by PDT_{ee} treatment (Fig. 4h and Supplementary Fig. 26a,b), which could result from gasdermin perforation in the mitochondrial membrane to augment caspase-3 activation[25]. Both caspase-3

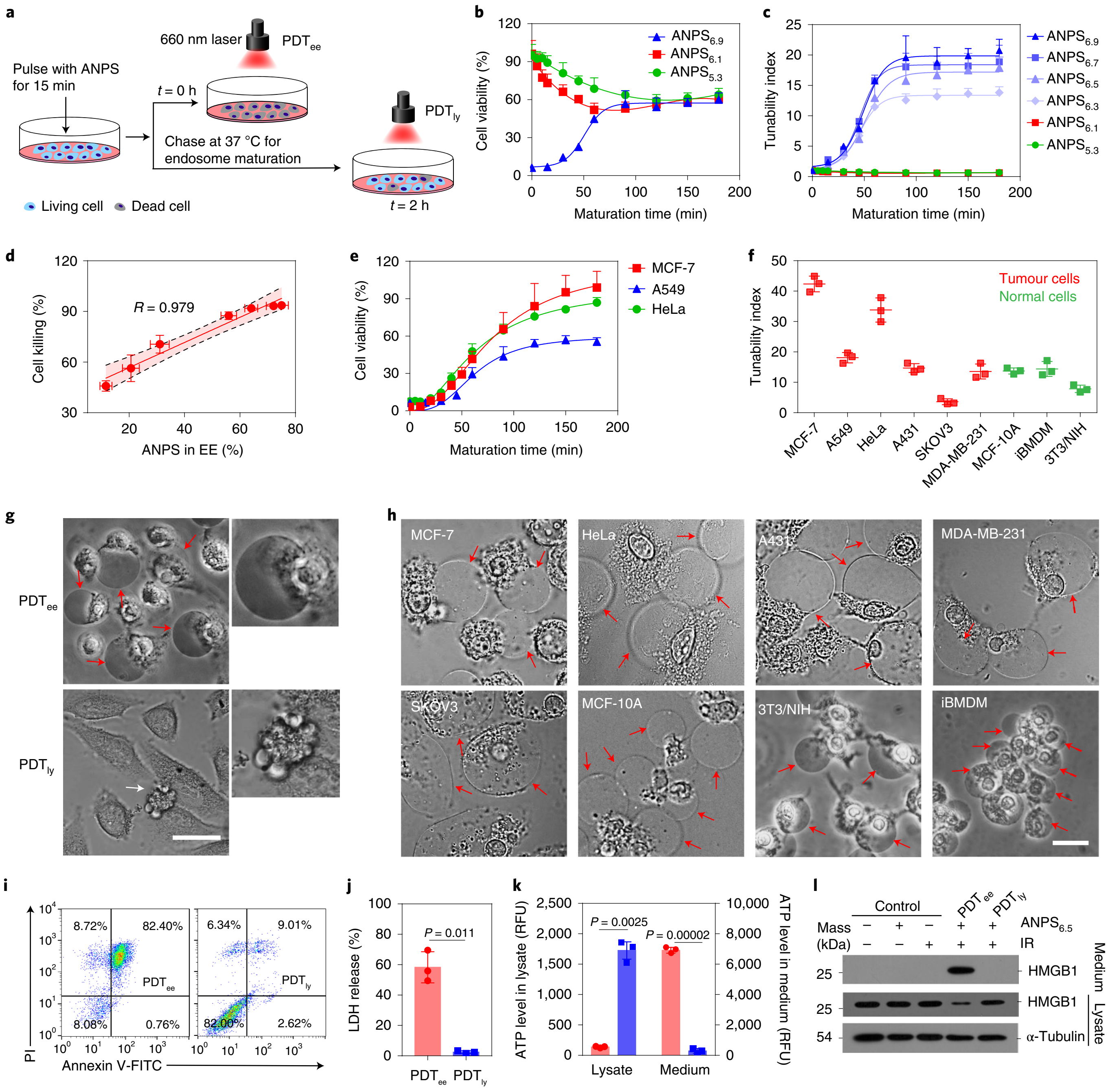

Fig. 3 | EE-targeted PDT achieves excellent anti-tumour efficacy via pyroptotic cell death. a, Schematic illustration of time-resolved cell photo-killing. Cells were pulsed with ANPS for 15 min and then chased at 37 °C for endosome maturation (0–3 h). Irradiation (100 mW cm^{-2} for 2 min) was carried out at specified time points (*t*); 0 h and 2 h were selected for PDT$_{ee}$ and PDT$_{ly}$, respectively. **b**, Temporal differentiation of endosome maturation on the efficacy of ANPS-library-mediated PDT. **c**, Tunability index of ANPS-library-mediated PDT during endosome maturation, as normalized to PDT$_{0h}$ (irradiation immediately post ANPS treatment). **d**, Positive correlation ($R = 0.979$) between the percentage of ANPS in EE (calculated from Supplementary Fig. 8d) and cell killing efficacy (calculated from Supplementary Fig. 12b). The error band in dashed lines and shading shows the 95% confidence intervals of the fitted line by two-sided Student's *t*-test analysis. **e**, Endosome maturation of intracellular ANPS weakens the PDT efficacy against various cancer cells, including A549, MCF-7 and HeLa cells. **f**, Tunability index of pyroptosis-inducing activity between EE and Ly on different cancerous and normal cells. iBMDM, immortalized bone-marrow-derived macrophage. **g**, Representative phase-contrast images of A549 cells treated with ANPS$_{6.5}$-mediated PDT$_{ee}$ or PDT$_{ly}$. Red and white arrows indicate the cells showing a pyroptotic or apoptotic morphology, respectively. Scale bar = 20 µm. The close-ups display the distinct cell death morphology induced by PDT$_{ee}$ and PDT$_{ly}$. **h**, Representative phase-contrast cell images of several tumour and normal cells treated with ANPS$_{6.5}$-mediated PDT$_{ee}$. Arrows mark the cells showing a pyroptotic morphology. Scale bar = 10 µm. **i**–**l**, Cell death nature of ANPS-mediated PDT. Representative flow cytometry of A549 cells stained with PI and Annexin V-FITC (**i**); LDH release (**j**); intra- and extracellular ATP level (**k**); and immunoblots of high-mobility group box 1 (HMGB1) in cell lysates or released in culture medium of A549 cells treated with PDT$_{ee}$ or PDT$_{ly}$, kDa is the mass unit of protein. (**l**). All data are presented as mean ± s.d. ($n = 3$ biologically independent experiments per group, two-sided Student's *t*-test with Welch's correction). RFU, relative fluorescence unit; IR, 660 nm laser irradiation.

inhibitors (Fig. 4i, Supplementary Fig. 27 and Supplementary Table 4) and genetic ablation (Supplementary Fig. 26c,d) blockaded the sensitivity to PDT_{ee}, as well as impeded GSDME cleavage and pyroptosis (Supplementary Fig. 26e,f). Altogether, ANPS-mediated PDT_{ee} can induce pyroptosis through caspase-3-mediated GSDME cleavage in GSDME-positive cells, whereas PDT-mediated apoptosis was found in GSDME-null cells and $GSDME^{-/-}$ cells.

Another pivotal issue that needs to be clarified is why the differential targeting of EE and Ly causes dramatically distinct cell killing efficacies. Several cellular stress responses have been elucidated during PDT, including lipid metabolism and calcium release[23]. Lipid peroxidation contributes to the phosphorylation and activation of PLC[26,27]. We discovered that with equivalent lipid metabolism (Supplementary Fig. 28a–c), only PDT_{ee} triggered PLC phosphorylation (Fig. 4j). Further investigation revealed that PLC was specifically localized in EE and gradually decreased in LE and Ly (Fig. 4k and Supplementary Fig. 28d), which has been reported in a previous study[28]. Notably, with PLC inhibitor U73122 (Fig. 4i and Supplementary Fig. 26) or genetic deletion of PLC (Fig. 4l and Supplementary Fig. 28e,f), PDT_{ee}-induced pyroptosis was significantly suppressed. Thus, PLC plays a critical role in pyroptosis stimulated by PDT_{ee}. Activated PLC can elevate the inositol 1,4,5-triphosphate (IP_3) level and thus increase the cytosolic concentration of calcium[29], initiating the mitochondrial apoptotic pathways mediated by cytochrome *c* and caspase-9 (refs. [30,31]). As expected, we observed an increase in IP_3 level (Supplementary Fig. 28g) and Ca^{2+} (Supplementary Fig. 29a–d and Supplementary Videos 5 and 6) induced by PDT_{ee} treatment, as well as the subsequent mitochondria stress and caspase-9 activation (Supplementary Figs. 29 and 30). Collectively, the underlying pyroptosis mechanism evoked by PDT_{ee} is elucidated in Fig. 4m. Apoptosis triggered by the released cathepsin B during lysosome membrane permeabilization is the dominant mechanism of lysosome photodamage[23,32]. We proved that cathepsin B was selectively accumulated in LE and Ly rather than in EE (Supplementary Fig. 31). PDT_{ly} induced lysosomal rupture (Supplementary Fig. 32), which triggered the leakage of cathepsins into cytosol to promote mild apoptosis with low cytotoxicity, at the same dose as that of PDT_{ee}. The poor sensitivity of Ly to reactive oxidative species stress is probably due to the following. First, the lysosomal membrane is highly glycosylated, which provides a protective layer at the membrane surface[33]. Second, the photooxidation of cathepsins (Supplementary Fig. 33)[34] and the neutral cytosol pH[35] caused dramatic activity loss for cathepsin B, leading to deficient apoptosis (Supplementary Fig. 34). However, robust apoptosis and cytotoxicity can be achieved by PDT_{ly} at a one-order-of-magnitude-higher dose of PDT_{ee} (Supplementary Fig. 12c,d).

ANPS achieves robust cancer ablation and minimized toxicity

Given the precise tunability and high efficiency of ANPS-mediated pyroptosis, we exploited this nanotuner for cancer therapy. $ANPS_{6.5}$ was chosen to optimize the in vivo drug-light intervals on an A549 model. Although longer circulation time led to higher tumour accumulation, the shorter drug-light intervals achieved significantly better tumour eradication (Fig. 5a and Supplementary Fig. 35). Irradiation at 3 h achieved the best anti-tumour efficacy among the predesignated drug-light intervals. In vivo tumour imaging revealed a rapid phase of cellular internalization and activation of ANPS within 3 h post-injection that allowed for the formation of numerous ANPS-contained EE, whereas the newly formed EE were dramatically attenuated from 6 to 24 h (slow phase) as indicated by the marginal enhancement of tumour fluorescent signals (Supplementary Fig. 36). The tumour section analyses further demonstrated that ANPS was highly colocalized with EE at 0.5–3 h and well colocalized with Ly at 6–24 h (Supplementary Fig. 37) due to endosome maturation and marginal new nanophotosensitizer internalization. As a proof of concept, we chose drug-light intervals of 3 h and 24 h for PDT_{ee} and PDT_{ly} in vivo, respectively. The PDT efficacy of the ANPS library was systematically investigated in A549 tumour-bearing mice. Results showed that $ANPS_{ee}$ (EE-targeted ANPS)-mediated PDT produced much better tumour inhibition (Fig. 5b and Supplementary Fig. 38) and prolonged survival time (Fig. 5c) than did $ANPS_{le}$ (LE-targeted ANPS)- or $ANPS_{ly}$ (Ly-targeted ANPS)-mediated PDT. $ANPS_{6.9}$ and $ANPS_{6.5}$ achieved 99.0% and 96.9% tumour eradication, respectively, significantly higher values than those of $ANPS_{6.1}$ (80.7%), $ANPS_{5.7}$ (55.3%) and $ANPS_{5.3}$ (51.9%; Fig. 5d). Hematoxylin and eosin (H&E) staining (Fig. 5e) and immunofluorescence staining (Supplementary Fig. 38c,d) of tumour sections also demonstrated more extensive cell death and cell proliferation inhibition by $ANPS_{ee}$ than by $ANPS_{le}$ and $ANPS_{ly}$. We further use the ANPS library for the treatment of an orthotopic MCF-7 mammary cancer model and achieved similar trends (Supplementary Fig. 39).

We then evaluated the anti-tumour efficacy of $ANPS_{6.5}$ on three orthotopic tumour models. Results revealed that PDT_{ee} almost removed the HN5, MCF-7 and A431 tumours without recurrence and animal death during the one-month treatment-free period (Fig. 5f–i and Supplementary Figs. 40–42). The percentages of tumour-free mice at the end of the studies were 42.9% (3/7), 40% (4/10) and 55.6% (5/9), respectively. Compared with PDT_{ee}, the efficacy of PDT_{ly} was dramatically compromised in all the tumour models. The residual tumour sizes treated with PDT_{ly} were 6.6-fold to 21.0-fold those treated with PDT_{ee} (Fig. 5j), a result that was further corroborated by TdT-mediated dUTP nick end labelling

Fig. 4 | PLC activation and caspase-3-mediated GSDME cleavage contribute to PDT_{ee}-induced pyroptosis. a, Immunoblots of GSDME cleavage of A549 cells treated with ANPS-library-mediated PDT. Ctr, control; GSDME-FL, full-length of GSDME. **b**, Immunoblots of maturation-time-dependent GSDME cleavage of A549 cells treated with $ANPS_{6.5}$-mediated PDT. **c**, Immunoblots of GSDME cleavage of A549, MCF-7, HeLa and SKOV3 cells treated with $ANPS_{6.5}$-mediated PDT_{ee} or PDT_{ly}. **d**, LDH release (two-sided Student's *t*-test with Welch's correction; $P = 0.11$ for wild type (WT) versus $GSDMD^{-/-}$; $P = 0.0038$ for WT versus $GSDME^{-/-}$). **e**, Representative cell morphology upon ANPS-mediated PDT in A549 cells with genetic ablation of GSDME or GSDMD. Scale bar = 20 µm. **f**, GSDME knockout ($GE^{-/-}$) rescued the anti-tumour efficacy of ANPS-mediated PDT_{ee} on orthotopic MCF-7 tumour model in vivo. Irradiation (660 nm, 100 mW cm^{-2} for 10 min) was carried out at 3 h post-administration of ANPS. Data are shown as mean ± s.d. ($n = 5$ biologically independent mice per group, two-sided Student's *t*-test with Welch's correction, $P = 0.00004$ for WT-PDT_{ee} versus $GSDME^{-/-}$-PDT_{ee}). PBS, phosphate-buffered saline. **g**, PDT_{ee} efficacy measured by MTT assay and immunoblots of GSDME expression in MCF-7 (high), SKOV3 (medium) and HT-29 (low) cells. **h**, Flow cytometry of real-time active caspase-3 staining in WT or $GSDME^{-/-}$ A549 cells with PDT_{ee} or PDT_{ly} treatments. **i**, Elucidation of the underlying mechanism of pyroptosis evoked by PDT_{ee} with the indicated inhibitors. **j**, Immunoblots of PLC-G1 (phospholipase C γ1) phosphorylation induced by $ANPS_{6.5}$-medidated PDT_{ee}. p-PLC-G1, phosphorylated PLC-G1. **k**, Representative confocal images of intracellular PLC-G1 (red); A549 cells were stained with RAB5A, RAB7A and LAMP1 (green) to investigate the colocalization of endocytic organelles with PLC-G1. Scale bar = 10 µm. **l**, MTT-assay-based cell viability and immunoblots of GSDME cleavage in WT or PLC-$G1^{-/-}$ A549 cells treated with PDT_{ee}. **m**, Illustration of possible GSDME-mediated pyroptosis mechanisms evoked by PDT_{ee}. Data are shown as mean ± s.d. ($n = 3$ biologically independent experiments per group) in all cell viability assays. 2-APB, 2-aminoethoxydiphenyl borate; IP_3R, inositol trisphosphate receptor; ER, endoplasmic reticulum; VAD, Z-VAD-FMK; DEVD, Z-DEVD-FMK.

(TUNEL) assay and H&E staining (Fig. 5k and Supplementary Figs. 40–42). The tunable pyroptosis and superior anti-tumour efficacy of ANPS-mediated PDT were also verified in the 4T1 tumour-bearing immunocompetent mouse model, accompanied with promotions on the number and function of tumour-infiltrating CD8$^+$ T cells (Supplementary Fig. 43). However, it is challenging to precisely control the tumour accumulation and subcellular localization of nanoparticles in vivo. Apart from the ANPS$_{ee}$-mediated pyroptosis that plays an important role in anti-tumour outcomes, other cell death models, including apoptosis and necrosis induced by diverse mechanisms, may also be involved in anti-cancer therapy in vivo.

Patients who have received clinical PDT treatment usually need to strictly avoid light for weeks to minimize undesired long-lasting phototoxicity to normal tissues[36]. Harnessing pH-responsive design and endosome maturation-tunable cytotoxicity, the ANPS could diminish the side effects without the need to strictly avoid light (Fig. 6a,b). In contrast to the Always-On nanoprobe, ANPS kept quenched fluorescence and SOG in fresh

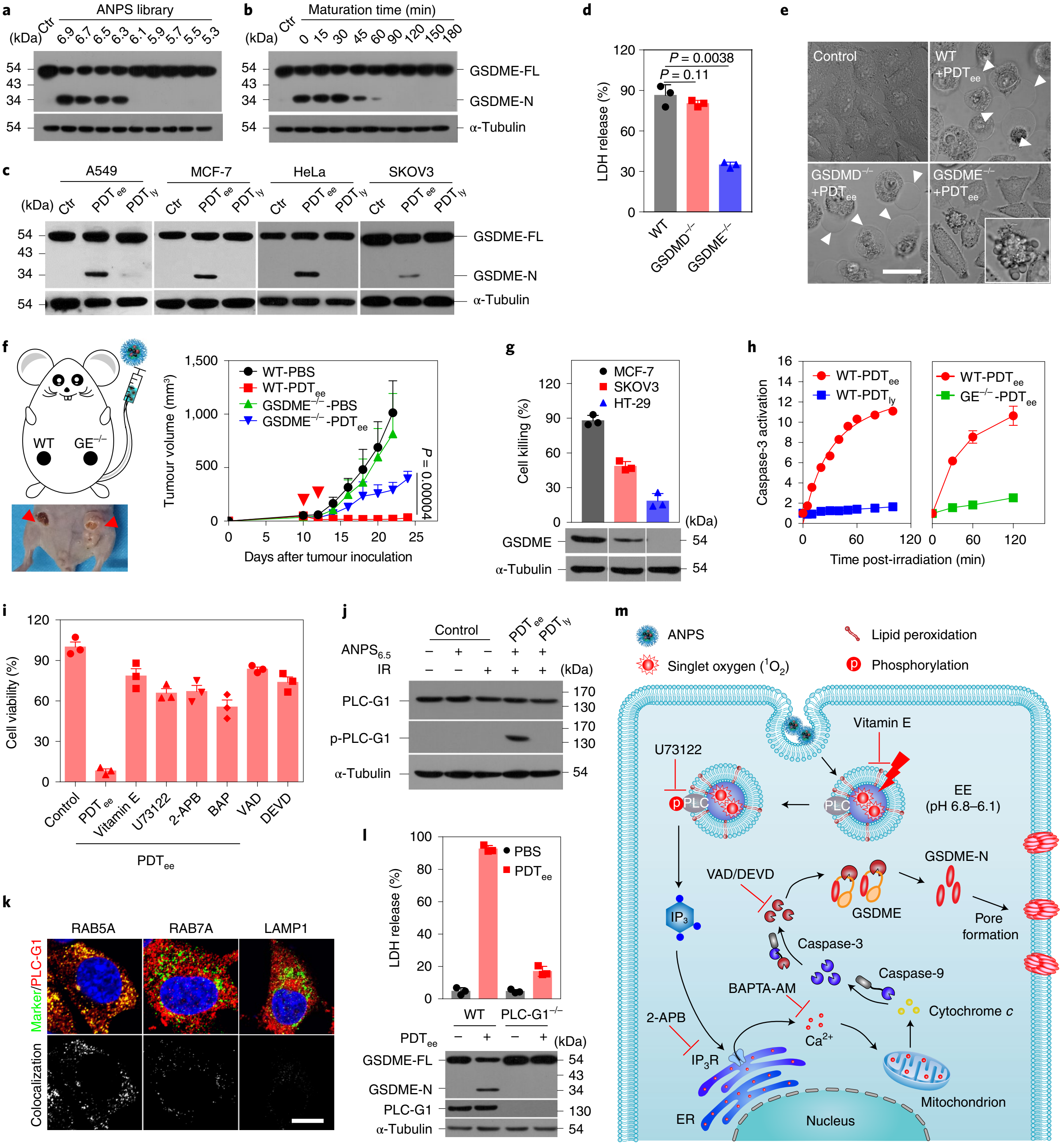

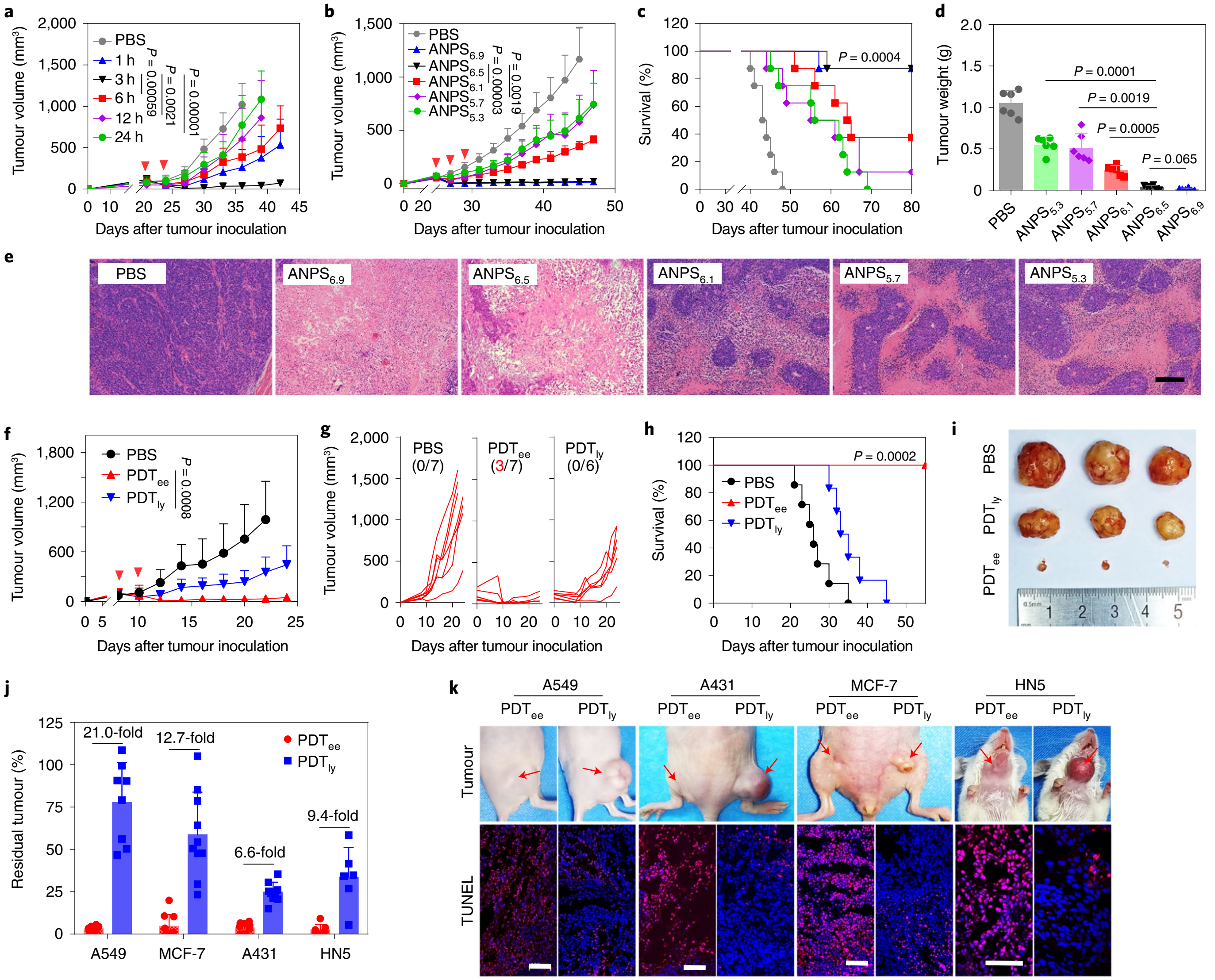

Fig. 5 | ANPS manipulates cellular distribution of photosensitizer for amplified photodynamic efficacy. a, Drug-light-interval-dependent PDT efficacy of $\mathrm{ANPS}_{6.5}$ on A549 tumour-bearing nu/nu nude mice in vivo ($n=8$ biologically independent mice per group; two-way analysis of variance (ANOVA) followed by Bonferroni's multiple comparisons test; $P=0.00059$ for 3 h versus 6 h, $P=0.0021$ for 3 h versus 12 h, $P=0.00001$ for 3 h versus 24 h). **b**–**e**, In vivo PDT efficacy of ANPS library on A549 tumour-bearing nu/nu nude mice. Tumour growth profiles (**b**; $n=8$ biologically independent mice per group; two-way ANOVA followed by Bonferroni's multiple comparisons test; $P=0.00003$ for $\mathrm{ANPS}_{6.5}$ versus $\mathrm{ANPS}_{6.1}$, $P=0.0019$ for $\mathrm{ANPS}_{6.5}$ versus $\mathrm{ANPS}_{5.7}$). Animal survival curves (**c**; log-rank test; $P=0.0004$ for $\mathrm{ANPS}_{6.5}$ versus $\mathrm{ANPS}_{5.3}$). Quantitative results of tumour weight excised at the end of the anti-tumour studies (**d**; $n=6$ biologically independent mice per group; two-sided Student's *t*-test; $P=0.065$ for $\mathrm{ANPS}_{6.5}$ versus $\mathrm{ANPS}_{6.9}$, $P=0.0005$ for $\mathrm{ANPS}_{6.5}$ versus $\mathrm{ANPS}_{6.1}$, $P=0.0019$ for $\mathrm{ANPS}_{6.5}$ versus $\mathrm{ANPS}_{5.7}$, $P=0.0001$ for $\mathrm{ANPS}_{6.5}$ versus $\mathrm{ANPS}_{5.3}$). Representative histological features of the tumour tissues two weeks after the last treatment (**e**). Scale bar = 100 μm. **f**–**i**, $\mathrm{ANPS}_{6.5}$-mediated PDT_{ee} exhibited excellent anti-tumour efficacy on orthotopic HN5 tumour-bearing non-obese diabetic (NOD) severe combined immunodeficient (SCID) mice as shown in tumour growth inhibition (**f**; $n=6$ mice for PDT_{ly} group; $n=7$ mice for other groups; two-sided Student's *t*-test with Welch's correction; $P=0.0008$ for PDT_{ee} versus PDT_{ly}). Individual tumour growth curves (**g**). Animal survival curves (**h**; log-rank test; $P=0.0002$ for PDT_{ee} versus PDT_{ly}. Excised tumours at day 24 (**i**). The red triangles indicate the time of administration. **j**, The residual tumour tissues relative to the PBS control ($n=8$ mice for A549 tumour; $n=10$ mice for MCF-7 tumour; $n=9$ mice for A431 tumour; $n=6$ mice for HN5 tumour). **k**, Photographs of tumour-bearing mice, as well as TUNEL staining (red) of slides in A549, A431, MCF-7 and HN5 tumour models. Scale bars = 100 μm. All data are shown as mean ± s.d. and all measurements (*n*) are biologically independent.

mice serum (Supplementary Fig. 44a,b), which resulted in negligible haemolysis (<3%) whether irradiated with a 660 nm laser or sunlight (Supplementary Fig. 44c,d). Moreover, the 'off' state of ANPS during blood circulation (Supplementary Fig. 45a–c) removed the irradiation-induced photodamage to blood cells and vessels (Fig. 6c–e and Supplementary Fig. 46), while exhibiting no allergies and good biocompatibility (Supplementary Fig. 45d–i). Our nanoprobes displayed 6.4-fold and 22.0-fold higher tumour internalizations than that in adjacent normal tissues in A549 and MCF-7 tumour models (Supplementary Fig. 47a,b), respectively, due to the enhanced permeability and retention effect and higher capacity of cell uptake in tumours as compared to normal tissues[19,37]. The high selectivity of ANPS towards cancer cells caused extensive tumour cell killing with reduced toxicity towards surrounding healthy tissues. Moreover, although the GSDME activity is genetically or epigenetically suppressed in several cancers[6], analysis with

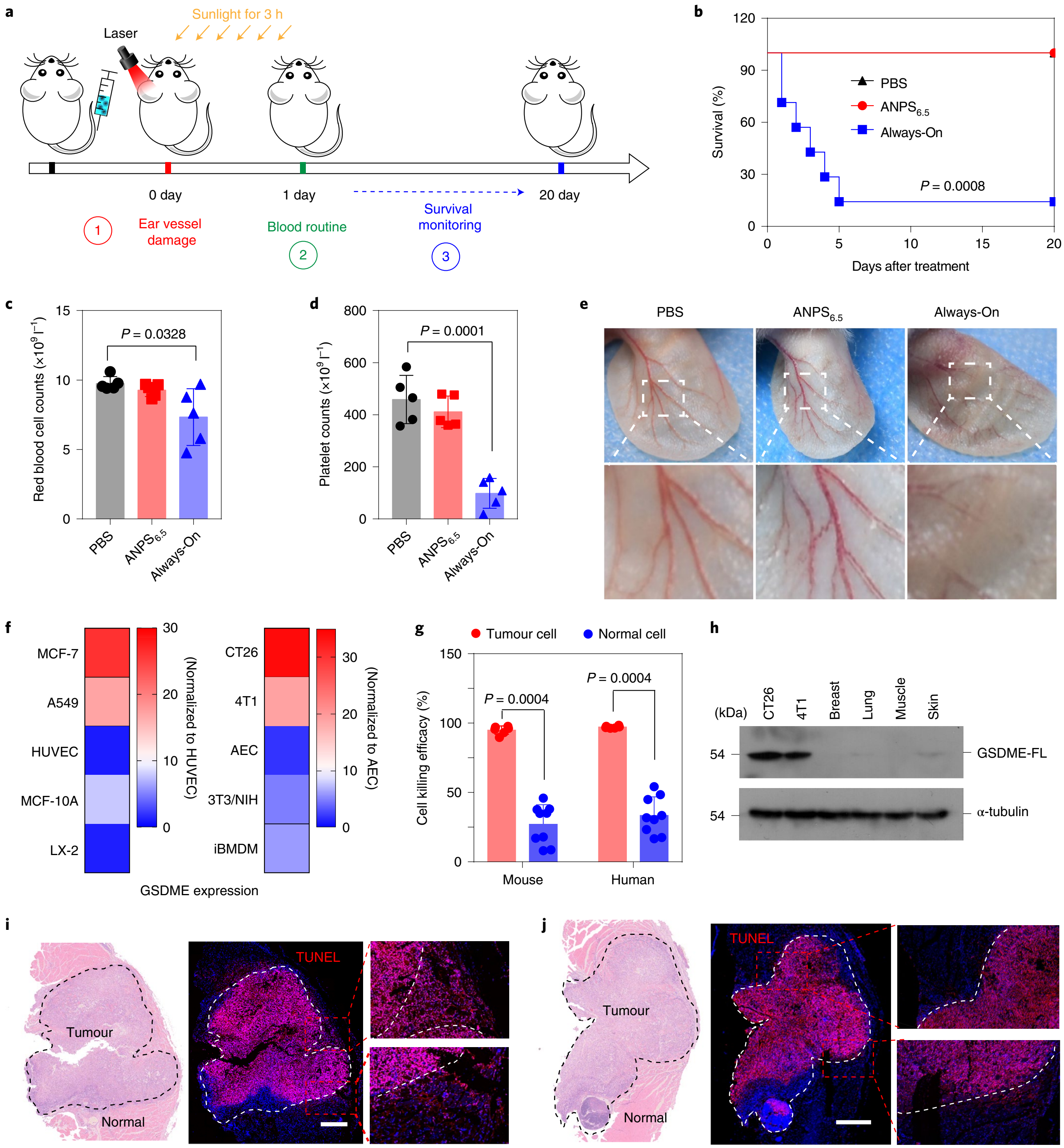

the Gene Expression Profiling Interactive Analysis (GEPIA) database revealed that nearly 50% of human tumour tissues have 1.5-fold to 39.8-fold higher expression than that in the corresponding normal tissue. Our results also revealed that cancer cell lines that expressed a higher level of GSDME than the normal cells presented high sensitivity to ANPS-mediated PDT_{ee} (Fig. 6f–h and Supplementary Fig. 47c–h). Given the high tumour-to-normal-tissue ratio (up to 20:1) for cell uptake of nanoprobes in vivo, the tumours with GSDME expression comparable to paired normal tissues are also suitable for ANPS-mediated PDT_{ee} treatment. Considering the heterogeneity and molecular background of human cancers, we can perform a patient stratification by pathological classification of the GSDME expression in clinical application. For the tumours with a high GSDME level, we can apply our pyroptosis nanotuner for efficient therapy. For the tumours with genetic or epigenetic suppression of GSDME, the DNA methyltransferase inhibitor (for example decitabine) can be applied to promote the expression of GSDME before PDT treatment (Supplementary Fig. 24). H&E and TUNEL assays indicated that the Always-On nanoprobe induced numerous incidences of necrosis and apoptosis in the adjacent muscle (Fig. 6i) and skin (Supplementary Fig. 48), whereas the toxicity was dramatically reduced due to the activatable property of ANPS (Fig. 6j).

Fig. 6 | ANPS minimizes phototoxicity by acid-activatable SOG and tunable pyroptosis. a, Experimental schedule for in vivo phototoxicity evaluation. Nu/nu nude mice were intravenous (i.v.) administered with PBS, ANPS$_{6.5}$ or Always-On at a Ce6 dose of 2.0 mg kg^{-1} and then exposed to sunlight irradiation for 3 h post-injection, and whole blood was collected 24 h after irradiation for a blood routine test. The survival of mice was monitored after irradiation. The phototoxicity to the blood vessel was investigated on the auricular vein with 660 nm irradiation (100 mW cm^{-2}). **b**, Survival curves of mice ($n=7$ biologically independent mice per group; log-rank test was applied for comparison; $P=0.0008$ for ANPS$_{6.5}$ versus Always-On). **c**,**d**, Red blood cell counts (**c**) and platelet counts (**d**) in whole blood. Data are shown as mean ± s.d. ($n=5$ biologically independent mice per group; two-tailed unpaired Student's *t*-test). **e**, Blood vessel damage on ear of nu/nu nude mice. **f**, Heat map showing the higher GSDME expression level in cancer cells than in normal cells. The alveolar epithelial cell (AEC) was primarily cultured from the lung tissue of a foetal mouse. HUVEC, human umbilical vein endothelial cells. **g**, ANPS$_{6.5}$-mediated PDT$_{ee}$ efficacy on different cancer cells and normal cells evaluated by MTT assay. Data are shown as mean ± s.d. ($n=3$ biologically independent experiments from two tumour cells and three normal cells; non-parametric test followed by Mann–Whitney test was used for comparison between two groups). **h**, GSDME expression in different tumour tissues and normal organs/tissues of tumour-bearing BALB/c mice measured by western blot. **i**, The Always-On nanoprobe exhibited serious phototoxicity on adjacent normal tissues measured by TUNEL imaging. Scale bar = 800 μm. **j**, ANPS-mediated PDT$_{ee}$ abolished the phototoxicity to the adjacent normal tissues measured by TUNEL imaging. Scale bar = 800 μm.

The toxicity of ANPS towards normal tissues can be further minimized after the nanoparticle transportation into Ly (Supplementary Fig. 49). However, the potential long-term toxicity of our ANPS needs to be comprehensively evaluated due to its non-biodegradable nature, which may limit its applicability in clinics[38]. Safe and biodegradable nanoparticles with pyroptosis tunability will be further investigated for biomedical applications.

Conclusions

In summary, we successfully produced a library of ANPSs, which spatiotemporally differentiate the endo-lysosomal pathway into ten distinct maturation stages with pH intervals of 0.2. The small ANPS library offers a powerful tool to introduce photodynamic oxidative stress into specific acidic endocytic regions, and further achieved location-dependent and organelle-specific tunability of pyroptotic cell death. We demonstrated that the nanoparticles elicit robust GSDME-mediated pyroptotic cancer cell death through a PLC-activated mitochondrial apoptosis pathway in EE, whereas their pyroptosis-inducing activity was suppressed in LE and Ly. The nanotuner strategy achieved robust pyroptotic killing against various GSDME-positive cancer cell types with reduced systemic toxicity. This study paves the way for the rational design of nanomedicines with pyroptosis-tuning activity for novel therapies based on targeting signalling of EE, but also offers new opportunities to explore nanomaterial-mediated pyroptosis for cancer immunotherapy.

Online content

Any methods, additional references, Nature Research reporting summaries, source data, extended data, supplementary information, acknowledgements, peer review information; details of author contributions and competing interests; and statements of data and code availability are available at https://doi.org/10.1038/s41565-022-01125-0.

Received: 22 October 2020; Accepted: 23 March 2022;
Published online: 23 May 2022

References

1. Bergsbaken, T., Fink, S. L. & Cookson, B. T. Pyroptosis: host cell death and inflammation. *Nat. Rev. Microbiol.* **7**, 99–109 (2009).
2. Shi, J. et al. Cleavage of GSDMD by inflammatory caspases determines pyroptotic cell death. *Nature* **526**, 660–665 (2015).
3. Broz, P., Pelegrin, P. & Shao, F. The gasdermins, a protein family executing cell death and inflammation. *Nat. Rev. Immunol.* **20**, 143–157 (2020).
4. Wang, Y. et al. Chemotherapy drugs induce pyroptosis through caspase-3 cleavage of a gasdermin. *Nature* **547**, 99–103 (2017).
5. Rogers, C. et al. Cleavage of DFNA5 by caspase-3 during apoptosis mediates progression to secondary necrotic/pyroptotic cell death. *Nat. Commun.* **8**, 14128 (2017).
6. Zhang, Z. et al. Gasdermin E suppresses tumour growth by activating anti-tumour immunity. *Nature* **579**, 415–420 (2020).
7. Wang, Q. et al. A bioorthogonal system reveals antitumour immune function of pyroptosis. *Nature* **579**, 421–426 (2020).
8. Mirshafiee, V. et al. Toxicological profiling of metal oxide nanoparticles in liver context reveals pyroptosis in Kupffer cells and macrophages versus apoptosis in hepatocytes. *ACS Nano* **12**, 3836–3852 (2018).
9. Reisetter, A. C. et al. Induction of inflammasome-dependent pyroptosis by carbon black nanoparticles. *J. Biol. Chem.* **286**, 21844–21852 (2011).
10. Zhang, X. et al. Mesoporous silica nanoparticles induced hepatotoxicity *via* NLRP3 inflammasome activation and caspase-1-dependent pyroptosis. *Nanoscale* **10**, 9141–9152 (2018).
11. Ploetz, E. et al. Metal–organic framework nanoparticles induce pyroptosis in cells controlled by the extracellular pH. *Adv. Mater.* **32**, e1907267 (2020).
12. Sorkin, A. & von Zastrow, M. Endocytosis and signalling: intertwining molecular networks. *Nat. Rev. Mol. Cell Biol.* **10**, 609–622 (2009).
13. Borkowska, M. et al. Targeted crystallization of mixed-charge nanoparticles in lysosomes induces selective death of cancer cells. *Nat. Nanotechnol.* **15**, 331–341 (2020).
14. Kim, S. E. et al. Ultrasmall nanoparticles induce ferroptosis in nutrient-deprived cancer cells and suppress tumour growth. *Nat. Nanotechnol.* **11**, 977–985 (2016).
15. Zhang, Y. et al. Tuning the autophagy-inducing activity of lanthanide-based nanocrystals through specific surface-coating peptides. *Nat. Mater.* **11**, 817–826 (2012).
16. He, B. et al. Single-walled carbon-nanohorns improve biocompatibility over nanotubes by triggering less protein-initiated pyroptosis and apoptosis in macrophages. *Nat. Commun.* **9**, 2393 (2018).
17. Ma, X. et al. Ultra-pH-sensitive nanoprobe library with broad pH tunability and fluorescence emissions. *J. Am. Chem. Soc.* **136**, 11085–11092 (2014).
18. Zhou, K. et al. Tunable, ultrasensitive pH-responsive nanoparticles targeting specific endocytic organelles in living cells. *Angew. Chem. Int. Ed.* **50**, 6109–6114 (2011).
19. Wang, Y. et al. A nanoparticle-based strategy for the imaging of a broad range of tumours by nonlinear amplification of microenvironment signals. *Nat. Mater.* **13**, 204–212 (2014).
20. Moan, J. & Berg, K. The photodegradation of porphyrins in cells can be used to estimate the lifetime of singlet oxygen. *Photochem. Photobiol.* **53**, 549–553 (1991).
21. Wang, C. et al. A nanobuffer reporter library for fine-scale imaging and perturbation of endocytic organelles. *Nat. Commun.* **6**, 8524 (2015).
22. Luo, M. et al. A STING-activating nanovaccine for cancer immunotherapy. *Nat. Nanotechnol.* **12**, 648–654 (2017).
23. Castano, A. P., Demidova, T. N. & Hamblin, M. R. Mechanisms in photodynamic therapy: part two—cellular signaling, cell metabolism and modes of cell death. *Photodiagnosis Photodyn. Ther.* **2**, 1–23 (2005).
24. Sun, L. et al. Mixed lineage kinase domain-like protein mediates necrosis signaling downstream of RIP3 kinase. *Cell* **148**, 213–227 (2012).
25. Rogers, C. et al. Gasdermin pores permeabilize mitochondria to augment caspase-3 activation during apoptosis and inflammasome activation. *Nat. Commun.* **10**, 1689 (2019).
26. Kang, R. et al. Lipid peroxidation drives gasdermin D-mediated pyroptosis in lethal polymicrobial sepsis. *Cell Host Microbe* **24**, 97–108.E4 (2018).
27. Agarwal, M. L., Larkin, H. E., Zaidi, S. I., Mukhtar, H. & Oleinick, N. L. Phospholipase activation triggers apoptosis in photosensitized mouse lymphoma cells. *Cancer Res.* **53**, 5897–5902 (1993).
28. Wang, Y. & Wang, Z. Regulation of EGF-induced phospholipase C-γ1 translocation and activation by its SH2 and PH domains. *Traffic* **4**, 618–630 (2003).

29. Lee, G. S. et al. The calcium-sensing receptor regulates the NLRP3 inflammasome through Ca^{2+} and cAMP. *Nature* **492**, 123–127 (2012).
30. Chen, K. et al. Deficiency in the membrane protein Tmbim3a/Grinaa initiates cold-induced ER stress and cell death by activating an intrinsic apoptotic pathway in zebrafish. *J. Biol. Chem.* **294**, 11445–11457 (2019).
31. Kuchay, S. et al. PTEN counteracts FBXL2 to promote $IP3R3^{-}$ and Ca^{2+}-mediated apoptosis limiting tumour growth. *Nature* **546**, 554–558 (2017).
32. Martins, W. K. et al. Parallel damage in mitochondria and lysosomes is an efficient way to photoinduce cell death. *Autophagy* **15**, 259–279 (2019).
33. Eskelinen, E. L., Tanaka, Y. & Saftig, P. At the acidic edge: emerging functions for lysosomal membrane proteins. *Trends Cell Biol.* **13**, 137–145 (2003).
34. Reiners, J. J. Jr, Agostinis, P., Berg, K., Oleinick, N. L. & Kessel, D. Assessing autophagy in the context of photodynamic therapy. *Autophagy* **6**, 7–18 (2010).
35. Sendler, M. et al. Cathepsin B activity initiates apoptosis via digestive protease activation in pancreatic acinar cells and experimental pancreatitis. *J. Biol. Chem.* **291**, 14717–14731 (2016).
36. Mitsunaga, M. et al. Cancer cell-selective in vivo near infrared photoimmunotherapy targeting specific membrane molecules. *Nat. Med.* **17**, 1685–1691 (2011).
37. Yin, Q. et al. Quantitative imaging of intracellular nanoparticle exposure enables prediction of nanotherapeutic efficacy. *Nat. Commum* **12**, 2385 (2021).
38. Wang, X. et al. Polycarbonate-based ultra-pH sensitive nanoparticles improve therapeutic window. *Nat. Commum* **11**, 5828 (2020).

Methods

Fabrication and characterization of ANPS library. The syntheses and characterization of block copolymers and dye conjugation are described in the Supplementary Methods. ANPS was formulated by a solvent evaporation method as reported previously[18]. Briefly, 2 mg of mixed Ce6-conjugated and QSY21-conjugated copolymers (1:1) were dissolved in 0.2 ml methanol. Then the solution was added dropwise into 4 ml Milli-Q deionized water under sonication. Micro-ultrafiltration tubes (100 kDa) were used to remove methanol with Milli-Q deionized water, and the copolymer concentration was adjusted to 5 mg ml^{-1} for further studies. For fabrication of the Always-On nanoprobe, the QSY21-conjugated copolymer was replaced with 3 equiv. dye-free copolymer to minimize the aggregation-caused quenching effect between Ce6 molecules.

For characterization, the particle size and zeta potential were measured by dynamic light scattering (Zetasizer Nano ZSP, Malvern) at 25 °C. The morphology and pH-induced micelle disassembly were confirmed by transmission electron microscopy (JEM-200CX, JEOL).

The pH-modulated fluorescence and SOG activation. The fluorescence off/on effect was evaluated by measuring the fluorescence emission spectra in a series of pH buffer solutions. In a typical procedure, 100 mM PBS buffers with different pH values were used to dilute the stock solution (5 mg ml^{-1}) of micelles to 100 µg ml^{-1}. The emission spectra were collected from 650 to 750 nm with excitation at 400 nm. The fluorescence intensity at 667 nm was employed to quantify the pH sensitivity and fluorescence off/on efficiency. Fluorescence off/on images of micelles were also captured with Living Image 4.3.1 (Lumina Series III, PerkinElmer) using an autoexposure model with bandpass filters ($\lambda_{ex}/\lambda_{em}$ refers to the wavelengths of excitation and emission, 620 ± 10 nm/670 ± 20 nm).

The SOG off/on efficiency was estimated by SOSG (Life Technology) and *p*-nitrosodimethylaniline, respectively. For the SOSG method, 5 mM SOSG stock solution was diluted with 100 µg ml^{-1} micelles at different pHs to a final concentration of 5.0 µM. The fluorescence intensity enhancement of SOSG (λ_{ex} = 494 nm and λ_{em} = 525 nm) before and after a 660 nm laser irradiation (MW-GX-660, 1,000 W, Laser Scientific; 100 mW cm^{-2} for 2 min) was measured as the SOG of the samples. For the *p*-nitrosodimethylaniline method, imidazole was used as the $^1O_2$ trapping agent, and the working concentrations of *p*-nitrosodimethylaniline and imidazole were 50 µM and 8 mM, respectively. The absorbance decrement at 440 nm of *p*-nitrosodimethylaniline before and after irradiation was detected as the SOG value. Vitamin C (2.5 mM) was applied as a singlet oxygen scavenger and was added before irradiation.

Stability, erythrocyte lysis assay and in vivo circulation. The details of the stability, erythrocyte lysis assay and in vivo circulation are described in the Supplementary Methods.

Cell culture. The A549 lung carcinoma (1101HUM-PUMC000002), MCF-7 (3101HUMSCSP531), MDA-MB-231 (1101HUM-PUMC000014) and 4T1 breast cancers (3101MOUSCSP5056); HeLa cervical carcinoma (1101HUM-PUMC000011); SKOV3 ovarian cancer (4201PAT-CCTCC01017); A431 epidermal carcinoma (1101HUM-PUMC000092); HT-29 (1101HUM-PUMC000109) and CT26 colon cancers (1101MOU-PUMC000275); HUVECs (4201PAT-CCTCC00692); 3T3/NIH fibroblast cells (1101MOU-PUMC000018); and normal human mammary epithelial cells (MCF-10A, 1101HUM-PUMC000406) were all purchased from National Infrastructure of Cell Line Resource. The human hepatic stellate cell line LX-2 was purchased from Xiangya School of Medicine, Central South University (Hunan, China). The immortalized bone-marrow-derived macrophage (iBMDM) was a gift from F. Shao of National Institute of Biological Sciences, Beijing. The caspase-3$^{-/-}$ HeLa cells were a gift from Z. Jiang of Peking University, Beijing. The HN5 head-neck cancer was a gift from J. Gao of the University of Texas Southwestern Medical Center (USA). The mouse AEC line was primary cultured from the lung tissues of foetal mouse. All cells except MCF-10A were cultured in DMEM medium with 10% foetal bovine serum (FBS) and antibiotics (penicillin 100 U ml^{-1} and streptomycin 100 µg ml^{-1}) at 37 °C with 5% CO_2. MCF-10A cells were cultured in MEBM medium supplemented with 100 ng ml^{-1} cholera toxin. All cells were tested to be negative for mycoplasma.

Cellular uptake, activation kinetics and subcellular trafficking. Cell lines and culture methods are described in the Supplementary Methods. For cellular uptake of the ANPS library, A549 cells were seeded in 12-well plates overnight for adherence and then incubated with $ANPS_{6.9}$, $ANPS_{6.1}$ and $ANPS_{5.3}$ (1.5, 3 and 6 µg ml^{-1} Ce6, respectively) for 15 min. After maturation at 37 °C in a 5% CO_2 atmosphere for another 2 h, the cells were trypsinized, harvested and washed with PBS. A CytoFLEX LX flow cytometer (FL4, APC channel, CytExpert 2.3, Beckman) was applied to quantify the cellular fluorescence of Ce6. To investigate the cellular fluorescence stability of ANPS, A549 cells were incubated with $ANPS_{6.5}$ (6 µg ml^{-1} Ce6) for 0.5 h, and then the cellular Ce6 fluorescence was determined at specified time points.

The pulse–chase method was applied to quantitate the cellular fluorescence activation kinetics of the ANPS library. A549 cells were incubated with nanophotosensitizers (6 µg ml^{-1} Ce6) for 5 min, and then washed with cold PBS immediately to prevent uptake and endosome maturation. Subsequently, the cell suspensions were kept at 37 °C with 5% CO_2 for endosome maturation, and the cellular fluorescence of Ce6 was real-time quantified by flow cytometer (FL4, APC channel). The activation kinetics curves were fitted with Origin 2018 software (Origin Lab) to calculate the 50% and 90% activation time of the ANPS library.

The intracellular activation, subcellular trafficking and colocalization studies of the ANPS library were further investigated by confocal laser scan microscopy (NIS-Elements AR 4.20.00, A1R-Storm, Nikon). A549 cells were transfected with CellLight Early Endosomes-RFP, Later Endosomes-GFP and Lysosomes-RFP BacMam 2.0 kits (Molecular Probes) for RAB5A (EE marker), RAB7A (LE marker) and LAMP1 (Ly marker) labelling, respectively. Nuclei were labelled with Hoechst 33342 (4 µg ml^{-1}, Molecular Probe) at 37 °C for 20 min. Then cells were incubated with $ANPS_{6.9}$, $ANPS_{6.1}$ or $ANPS_{5.3}$ at a Ce6 concentration of 6 µg ml^{-1} (diluted with culture medium) at 37 °C for 15 min. After being replaced with fresh medium, subcellular localization of Ce6 was captured at designated time points by confocal fluorescence microscopy. The 4′,6-diamidino-2-phenylindole (DAPI), FITC, tetramethylrhodamine (TRITC) and Cy5 filters were used for Hoechst 33342, GFP, RFP and Ce6 imaging, respectively. The colocalizations of Ce6 with organelles were analysed with ImageJ software (NIH).

CRISPR-Cas9 knockout cells and GFP transfection. GSDME$^{-/-}$, GSDMD$^{-/-}$ and PLC-G1$^{-/-}$ A549 cells; GSDME$^{-/-}$ MCF-7 cells; GSDME$^{-/-}$ HeLa cells; GSDME$^{-/-}$ A431 cells; and GFP-labelled cells were all constructed by CRISPR-Cas9 technology as described in the Supplementary Methods.

In vitro evaluation of PDT efficacy. The cellular SOG of ANPS was measured by a modified SOSG nanosensor developed by our laboratory as described in the Supplementary Methods. For the in vitro PDT effect, A549 cells were seeded on a 24-well plate at a density of 2×10^4 cells per well and incubated for 24 h at 37 °C before the assay. The culture medium was then replaced with fresh medium containing a series of Ce6 concentrations of the ANPS library. After 15 min incubation at 37 °C, the ANPS-containing medium was removed, and fresh culture medium without phenol red was added. Irradiation (660 nm, 100 mW cm^{-2} for 2 min) was carried out for 0 h ($ANPS_{6.9}$, $ANPS_{6.7}$, $ANPS_{6.5}$, $ANPS_{6.3}$), 1 h ($ANPS_{6.1}$, $ANPS_{5.9}$, $ANPS_{5.7}$) or 2 h ($ANPS_{5.5}$, $ANPS_{5.3}$). The MTT assay was carried out to measure the cell viability 24 h after irradiation. Briefly, 0.5 ml MTT solution (at a final concentration of 0.5 mg ml^{-1}) was added to the wells, and the generated formazan was dissolved with DMSO solvent after 1 h incubation. The absorbance was quantified at 540 nm on a microplate reader (Multiskan FC, Thermo Fisher Scientific). The IC_{50} values of the nanophotosensitizer library on A549 cells were calculated by Origin Pro software. MCF-7 and HeLa cells were also included to compare the PDT efficacy of the ANPS library. Calcein AM (2 µM, Santa Cruz) and PI (4.5 µM, Sigma) were used to label cells for 30 min to distinguish living cells and dead cells, respectively, and the cells were visualized with confocal laser scan microscopy. The cell death mechanism was investigated by an Annexin V-FITC/PI Apoptosis Detection Kit (Beyotime) according to the manufacturer's instructions 6 h after irradiation, and analysed using fluorescence-activated cell sorting. The PDT efficacies of ANPS, Always-On nanoprobe and free Ce6 during endosome maturation were also evaluated, as described in the Supplementary Methods.

Microscope imaging of cell death. To observe the cell morphology with different treatments, cells were seeded in glass-bottom dishes at about 50% confluence and subjected to the indicated treatments for static image capture and living imaging. Representative bright-field images of cell death were observed and captured with a Zeiss Axio Vert AI or Zeiss LSM880 (ZEN 2010) confocal microscope. The images were processed with ImageJ 1.47 software. Live images of cell death after the indicated treatments were also recorded in real time by a Zeiss LSM880 confocal microscope and processed with Corel VideoStudio X10 program. Cells were transfected with GFP (CRISPR-Cas9 technology) or stained with PI (1 µM) to indicate the integrity of the cell membrane. All image data are shown as representative of at least three randomly selected fields.

Immunoblot analysis. The cellular expression of HMGB1, α-tubulin, PLC-G1, RIP-1, RIP-3, MLKL, GPX4, cleavages of GSDME, cleavages of GSDMD and activations of caspase-3 were all detected by western blot analysis. Cells with different treatments were lysed in buffer containing 25 mM tris(hydroxymethyl) aminomethane (Tris; pH 7.4), 150 mM NaCl, 0.5% sodium deoxycholate, 0.1% SDS buffer and 1% Triton X-100 surfactant, as well as cocktail protease inhibitor (Roche) and phosphatase inhibitor (Roche). Cell lysates were clarified by spinning at 13,800*g* for 10 min at 4 °C, and supernatants were diluted with ×4 loading buffer, followed by boiling for 10 min. Denatured proteins (20 µg) were fractionated by sodium dodecyl sulfate–polyacrylamide gel electrophoresis and transferred to polyvinyl difluoride membranes with a Mini-PROTEAN Tetra system (Bio-Rad). Blots were then blocked with 5% skim milk in Tris-buffered saline plus 0.05% Tween-20 and probed with appropriate antibodies according to the manufacturer's instructions. To examine the released HMGB1, culture supernatants of cells with different treatments were collected and centrifugated at 13,800*g* for 10 min at 4 °C to remove dead cells. The supernatants were then diluted with ×4 loading buffer and boiled for 10 min. The obtained proteins were fractionated by 12% sodium dodecyl sulfate–polyacrylamide gel electrophoresis followed with electroblotting onto polyvinyl difluoride membranes.

Inhibitor treatments. To elucidate the mechanism of PDT_{ee}-induced cell death, A549 cells were pretreated with various inhibitors (Supplementary Table 4) 24 h before PDT_{ee}, including antioxidant vitamin E (100 µM), PLC inhibitor U73122 (10 µM), IP_3 receptor inhibitor 2-aminoethoxydiphenyl borate (20 µM), calcium chelator BAPTA-AM (20 µM), pan-caspase inhibitor Z-VAD-FMK (50 µM), specific caspase-3 inhibitor Z-DEVD-FMK (50 µM), necroptosis inhibitor necrostation-1 (50 µM), cathepsin inhibitor leupeptin (4 µM) and ferroptosis inhibitors ferrostatin-1 (0.5 µM) and liproxstatin-1 (0.5 µM). MTT assay, LDH release assay and caspase-3 activation were applied to evaluate the rescue efficacy. To investigate the effect of DNA methyltransferase inhibitor on PDT_{ee}, SKOV3 cells were treated with 5 µM decitabine for seven days. Immunoblotting was used to detect GSDME expression after decitabine treatment. MTT assay and LDH release assay were applied to verify the effect of DNA methyltransferase on PDT_{ee}-evoked pyroptosis.

Intracellular biochemical analysis. Lipid peroxidation probe C11-BODIPY$^{581/591}$ (Invitrogen) was used to detect intracellular lipid peroxide by flow cytometry and confocal microscopy[39]. A549 cells were treated with PBS, $ANPS_{6.5}$-mediated PDT_{ee} or $ANPS_{6.5}$-mediated PDT_{ly}, and then stained with 2 µM C11-BODIPY$^{581/591}$ for 0.5 h after irradiation. Cellular lipid peroxide was then quantified and captured by flow cytometry and confocal microscopy, respectively. Malondialdehyde (ab118970, Abcam; the oxidative degradation product of lipids) and IP_3 (CEC037Ge, Cloud-Clone; the enzyme degradation product of PLC) were both measured after irradiation according to the manufacturer's protocols[26]. The intracellular glutathione peroxidase 4 activity, caspase activity, calcium signal and mitochondria stress after PDT treatment were all determined with assay kits according to the manufacturer's protocols as described in the Supplementary Methods.

In vivo anti-tumour study. Female nu/nu nude mice (6–8 weeks), NOD–SCID mice (6–8 weeks) and BALB/c mice (6–8 weeks) were purchased from Vital River Laboratory Animal Center (China) and kept under specific pathogen free conditions for one week before the studies, with free access to standard food and water. All care and handling of animals were performed with the approval of the Ethics Committee of Peking University (protocol number LA2019039). Animals were housed in groups of 4–5 mice per cage, maintained at a temperature of ~25 °C in a humidity-controlled environment with a 12 h light/dark cycle. Tumour models are described in the Supplementary Methods. The maximum permitted tumour volume (2,000 mm^3) was not exceeded in any study. For the PDT efficacy of the ANPS library, orthotopic MCF-7 or subcutaneous A549 tumour-bearing nu/nu nude mice were randomly divided into six groups ($n = 6$–8) and treated with PBS, $ANPS_{6.9}$, $ANPS_{6.5}$, $ANPS_{6.1}$, $ANPS_{5.7}$ and $ANPS_{5.3}$ at an equal Ce6 dose of 2.0 mg kg^{-1} via tail vein. Mice were anaesthetized with 1.2% avertin, and the tumour sites were irradiated with a 660 nm laser (240 J cm^{-2}) at a specified time point post-injection (3 h for $ANPS_{6.9}$ and $ANPS_{6.5}$, 12 h for $ANPS_{6.1}$ and $ANPS_{5.7}$, 24 h for $ANPS_{5.3}$). The treatments were repeated every two days, three times. By monitoring tumour growth, mice were euthanized once the tumours had reached ~1,500 mm^3 in size.

For the tumour inhibition of PDT_{ee} and PDT_{ly}, A549 tumour-bearing nu/nu nude mice were randomly divided into six groups, and five groups were i.v. treated with $ANPS_{6.5}$ (2.0 mg kg^{-1} Ce6). Irradiation (240 J cm^{-2}) was carried out 1 h, 3 h, 6 h, 12 h and 24 h post-injection. The treatment was repeated every two days, twice. Orthotopic MCF-7 (nu/nu nude mice), HN5 (NOD–SCID mice), subcutaneous A431 (nu/nu nude mice) and 4T1 (BALB/c mice) tumour-bearing mice were also randomly divided into three or four groups, and respectively treated with PBS, IR, PDT_{ee} (irradiation at 3 h post-injection) or PDT_{ly} (irradiation at 24 h post-injection). The treatments were repeated every two days, twice. The tumour size and mouse weight were measured every other day. Tumour tissues were excised, weighed and imaged at the end of the study. Frozen sections of tumours were prepared for in situ apoptosis analysis by TUNEL assay according to the manufacturer's instructions. Paraffin section of tumours were also prepared for histological study by H&E staining.

For in vivo mechanism verification of PDT_{ee}, wild-type and GSDME$^{-/-}$ A549 cells or MCF-7 cells were inoculated on the left and right flanks or breast pads of the same nu/nu nude mice, respectively. Bilateral tumour-bearing mice were randomly divided into two groups and treated with PBS or $ANPS_{6.5}$-mediated PDT_{ee}. The treatments were repeated every two days, twice.

In vivo phototoxicity and biocompatibility study. For the phototoxicity study in vivo, nu/nu nude mice ($n = 7$) were i.v. administered with PBS, $ANPS_{6.5}$ or Always-On at a Ce6 dose of 2.0 mg kg^{-1} every two days, twice. Mice were exposed to solar irradiation for 3 h post-injection. Whole blood and serum were collected from the orbit of each mouse 24 h after the second irradiation for blood routine and biochemistry tests, respectively. The survival of the mice was monitored after irradiation. The phototoxicity to the blood vessel was also investigated on an auricular vein with 660 nm irradiation (100 mW cm^{-2}) and recorded by a digital camera. For phototoxicity to normal tissues adjacent to tumours, A549 cells were intramuscularly injected at the bilateral flank of nu/nu nude mice. $ANPS_{6.5}$ or Always-On nanoprobes were injected via tail vein at a Ce6 dose of 2 mg kg^{-1}, and irradiation (240 J cm^{-2}) was carried out at tumour sites including adjacent normal tissues at 3 h (left flank) or 24 h (right flank). The tumour tissues and adjacent normal tissues were together excised at 24 h post-irradiation, and sectioned for histological study and TUNEL assay.

For the biocompatibility study, BALB/c mice ($n = 6$) were i.v. administered with PBS or 50 mg kg^{-1} or 100 mg kg^{-1} $ANPS_{6.5}$ at day 0. The body weight of the mice was measured for two weeks, and the major organs were excised for H&E staining at day 20.

Statistics and reproducibility. Data are presented as mean ± s.d. for in vitro and in vivo assays. Statistical analyses were performed using Origin (Origin 2018). An independent-sample t-test or one-way (or two-way) ANOVA followed by Bonferroni's multiple comparisons test were conducted for analysis of significant differences depending on the number and distribution of treatment groups. Welch's correction or non-parametric test was applied for the groups without equal s.d. A log-rank test was applied for comparison of survival curves; $P < 0.05$ was considered significant. Each experiment, including transmission electron microscopy, confocal imaging, cell morphology assay and western blot, was independently repeated at least thrice with similar results. The in vivo imaging, immunofluorescence staining of tissues and H&E staining were repeated three times using biologically independent mice with similar results.

Reporting summary. Further information on research design is available in the Nature Research Reporting Summary linked to this article.

Data availability

Source data are provided with this paper. The main data that support the findings of this study are available within the paper, the source data and the Supplementary Information. The GEPIA database is accessible via http://gepia.cancer-pku.cn/. Other raw and relevant data from the study are available for research purposes from the corresponding authors upon reasonable request.

References

39. Wang, S. et al. Arginine-rich manganese silicate nanobubbles as a ferroptosis-inducing agent for tumor-targeted theranostics. *ACS Nano* **12**, 12380–12392 (2018).

Acknowledgements

This work was supported by the National Key Research and Development Program of China (2017YFA0205600 and 2016YFA0201400 to Yiguang Wang), National Natural Science Foundation of China grants (81622046 and 81973260 to Yiguang Wang and 81903554 to B.C.) and the Beijing Natural Science Foundation (JQ19025 to Yiguang Wang).

Author contributions

B.C. and Yiguang Wang are responsible for all phases of the research. Y. Yan, Yaoqi Wang and F.W. helped with the characterization and efficacy evaluation of the nanophotosensitizer library. Z.W. helped with the synthesis and characterization of copolymers. X.W., Y.L. and L.W. performed the CRISPR-Cas9 knockout cell lines. Y. Yang and G.C. participated in the western blot. Q.Y. and B.X. performed the in vitro cell imaging and in vivo imaging. B.C. and Yiguang Wang wrote the manuscript. F.Y., Q.Z. and Yiguang Wang provided conceptual advice and supervised the study. All the authors discussed the results and assisted in the preparation of the manuscript.

Competing interests

The authors declare no competing interests.

Additional information

Supplementary information The online version contains supplementary material available at https://doi.org/10.1038/s41565-022-01125-0.

Correspondence and requests for materials should be addressed to Fuping You, Qiang Zhang or Yiguang Wang.

Peer review information *Nature Nanotechnology* thanks Xiaoyuan Chen, Roger Gomis and the other, anonymous, reviewer(s) for their contribution to the peer review of this work.

Reprints and permissions information is available at www.nature.com/reprints.

nature research

Corresponding author(s): Yiguang Wang

Last updated by author(s): Feb 21, 2022

Reporting Summary

Nature Research wishes to improve the reproducibility of the work that we publish. This form provides structure for consistency and transparency in reporting. For further information on Nature Research policies, see our Editorial Policies and the Editorial Policy Checklist.

Statistics

For all statistical analyses, confirm that the following items are present in the figure legend, table legend, main text, or Methods section.

n/a	Confirmed	
☐	☒	The exact sample size (*n*) for each experimental group/condition, given as a discrete number and unit of measurement
☐	☒	A statement on whether measurements were taken from distinct samples or whether the same sample was measured repeatedly
☐	☒	The statistical test(s) used AND whether they are one- or two-sided *Only common tests should be described solely by name; describe more complex techniques in the Methods section.*
☒	☐	A description of all covariates tested
☐	☒	A description of any assumptions or corrections, such as tests of normality and adjustment for multiple comparisons
☐	☒	A full description of the statistical parameters including central tendency (e.g. means) or other basic estimates (e.g. regression coefficient) AND variation (e.g. standard deviation) or associated estimates of uncertainty (e.g. confidence intervals)
☐	☒	For null hypothesis testing, the test statistic (e.g. *F*, *t*, *r*) with confidence intervals, effect sizes, degrees of freedom and *P* value noted *Give P values as exact values whenever suitable.*
☒	☐	For Bayesian analysis, information on the choice of priors and Markov chain Monte Carlo settings
☒	☐	For hierarchical and complex designs, identification of the appropriate level for tests and full reporting of outcomes
☐	☒	Estimates of effect sizes (e.g. Cohen's *d*, Pearson's *r*), indicating how they were calculated

Our web collection on statistics for biologists contains articles on many of the points above.

Software and code

Policy information about availability of computer code

Data collection	ZEN 2010 was used for LSM 880 (Zeiss); NIS-Elements AR 4.20.00 was used for A1R-Storm (Nikon); Living Image 4.3.1 was used for Lumina Series III (PerkinElmer); CytExpert 2.3 was used for CytoFLEX LX (Beckman); MestReNova 9.0 was applied for 1H-NMR.
Data analysis	1H-NMR data was analyzed by MestReNova 9.0; Statistical analyses were performed on Origin 2018; Flow cytometry data were analyzed on FlowJo software package (Flowjo V10); Curves were fitted with Origin 2018; Images were processed with Image-J 1.47 software (NIH); Videos were processed with Corel VideoStudio X10 program.

For manuscripts utilizing custom algorithms or software that are central to the research but not yet described in published literature, software must be made available to editors and reviewers. We strongly encourage code deposition in a community repository (e.g. GitHub). See the Nature Research guidelines for submitting code & software for further information.

Data

Policy information about availability of data

All manuscripts must include a data availability statement. This statement should provide the following information, where applicable:

- Accession codes, unique identifiers, or web links for publicly available datasets
- A list of figures that have associated raw data
- A description of any restrictions on data availability

The source data underlying Figure 2, Figure 3, Figure 4, Figure 5, Figure 6, and western bot are provided with this paper. The main data that support the findings of this study are available within the paper, source data and its Supplementary Information. GEPIA database is accessible via http://gepia.cancer-pku.cn/. Other raw and relevant data during the study are available for research purposes from the corresponding authors upon reasonable request.

Field-specific reporting

Please select the one below that is the best fit for your research. If you are not sure, read the appropriate sections before making your selection.

☒ Life sciences ☐ Behavioural & social sciences ☐ Ecological, evolutionary & environmental sciences

For a reference copy of the document with all sections, see nature.com/documents/nr-reporting-summary-flat.pdf

Life sciences study design

All studies must disclose on these points even when the disclosure is negative.

Sample size	Sample size was chosen to ensure reproducibility of the experiments in accordance with the replacement, reduction and refinement principles of animal ethics regulation. Sample sizes employed in this study are consistent with previously published works (Nature Nanotechnology 2021, 16(12): 1394-1402; Nature Nanotechnology 2019, 14(8): 799-809).
Data exclusions	No animals and/or data were excluded.
Replication	All experiments were repeated for at least three times and experimental findings were reproducible. Details of experimental replicates are given in the figure legends.
Randomization	All experimental samples or models including in vitro cells and in vivo mice were randomly allocated to each group.
Blinding	No blinding was performed in this study. The investigators should keep careful track of protocols because that most of the experiments needed multiple treatments (including formulation, cells or mouse tumor treatment, sample collection, and so on). Hence, it would be difficult to blind the investigators to group allocation during data collection and analysis.

Behavioural & social sciences study design

All studies must disclose on these points even when the disclosure is negative.

Study description	*Briefly describe the study type including whether data are quantitative, qualitative, or mixed-methods (e.g. qualitative cross-sectional, quantitative experimental, mixed-methods case study).*
Research sample	*State the research sample (e.g. Harvard university undergraduates, villagers in rural India) and provide relevant demographic information (e.g. age, sex) and indicate whether the sample is representative. Provide a rationale for the study sample chosen. For studies involving existing datasets, please describe the dataset and source.*
Sampling strategy	*Describe the sampling procedure (e.g. random, snowball, stratified, convenience). Describe the statistical methods that were used to predetermine sample size OR if no sample-size calculation was performed, describe how sample sizes were chosen and provide a rationale for why these sample sizes are sufficient. For qualitative data, please indicate whether data saturation was considered, and what criteria were used to decide that no further sampling was needed.*
Data collection	*Provide details about the data collection procedure, including the instruments or devices used to record the data (e.g. pen and paper, computer, eye tracker, video or audio equipment) whether anyone was present besides the participant(s) and the researcher, and whether the researcher was blind to experimental condition and/or the study hypothesis during data collection.*
Timing	*Indicate the start and stop dates of data collection. If there is a gap between collection periods, state the dates for each sample cohort.*
Data exclusions	*If no data were excluded from the analyses, state so OR if data were excluded, provide the exact number of exclusions and the rationale behind them, indicating whether exclusion criteria were pre-established.*
Non-participation	*State how many participants dropped out/declined participation and the reason(s) given OR provide response rate OR state that no participants dropped out/declined participation.*

Randomization	*If participants were not allocated into experimental groups, state so OR describe how participants were allocated to groups, and if allocation was not random, describe how covariates were controlled.*

Ecological, evolutionary & environmental sciences study design

All studies must disclose on these points even when the disclosure is negative.

Study description	*Briefly describe the study. For quantitative data include treatment factors and interactions, design structure (e.g. factorial, nested, hierarchical), nature and number of experimental units and replicates.*
Research sample	*Describe the research sample (e.g. a group of tagged Passer domesticus, all Stenocereus thurberi within Organ Pipe Cactus National Monument), and provide a rationale for the sample choice. When relevant, describe the organism taxa, source, sex, age range and any manipulations. State what population the sample is meant to represent when applicable. For studies involving existing datasets, describe the data and its source.*
Sampling strategy	*Note the sampling procedure. Describe the statistical methods that were used to predetermine sample size OR if no sample-size calculation was performed, describe how sample sizes were chosen and provide a rationale for why these sample sizes are sufficient.*
Data collection	*Describe the data collection procedure, including who recorded the data and how.*
Timing and spatial scale	*Indicate the start and stop dates of data collection, noting the frequency and periodicity of sampling and providing a rationale for these choices. If there is a gap between collection periods, state the dates for each sample cohort. Specify the spatial scale from which the data are taken*
Data exclusions	*If no data were excluded from the analyses, state so OR if data were excluded, describe the exclusions and the rationale behind them, indicating whether exclusion criteria were pre-established.*
Reproducibility	*Describe the measures taken to verify the reproducibility of experimental findings. For each experiment, note whether any attempts to repeat the experiment failed OR state that all attempts to repeat the experiment were successful.*
Randomization	*Describe how samples/organisms/participants were allocated into groups. If allocation was not random, describe how covariates were controlled. If this is not relevant to your study, explain why.*
Blinding	*Describe the extent of blinding used during data acquisition and analysis. If blinding was not possible, describe why OR explain why blinding was not relevant to your study.*

Did the study involve field work? ☐ Yes ☐ No

Field work, collection and transport

Field conditions	*Describe the study conditions for field work, providing relevant parameters (e.g. temperature, rainfall).*
Location	*State the location of the sampling or experiment, providing relevant parameters (e.g. latitude and longitude, elevation, water depth).*
Access & import/export	*Describe the efforts you have made to access habitats and to collect and import/export your samples in a responsible manner and in compliance with local, national and international laws, noting any permits that were obtained (give the name of the issuing authority, the date of issue, and any identifying information).*
Disturbance	*Describe any disturbance caused by the study and how it was minimized.*

Reporting for specific materials, systems and methods

We require information from authors about some types of materials, experimental systems and methods used in many studies. Here, indicate whether each material, system or method listed is relevant to your study. If you are not sure if a list item applies to your research, read the appropriate section before selecting a response.

Materials & experimental systems

n/a	Involved in the study	
☐	☒	Antibodies
☐	☒	Eukaryotic cell lines
☒	☐	Palaeontology and archaeology
☐	☒	Animals and other organisms
☒	☐	Human research participants
☒	☐	Clinical data
☒	☐	Dual use research of concern

Methods

n/a	Involved in the study	
☒	☐	ChIP-seq
☐	☒	Flow cytometry
☒	☐	MRI-based neuroimaging

Antibodies

Antibodies used

The anti-Ki-67 (Cat. No. ab15580), anti-HMGB1 (Cat. No. ab79823), anti-GSDME (Cat. No. ab215191), anti-GSDMD (Cat. No. ab210070), anti-RIP1 (Cat. No. ab125072), anti-p-RIP3 (Cat. No. ab209384), anti-MLKL (Cat. No. ab184718), anti-p-MLKL (Cat. No. ab187091), anti-GPX4 (Cat. No. ab125066), anti-PLC-G1(Cat. No. ab107455), anti-p-PLC-G1 (Cat. No. ab76031), anti-Rab 5a (Cat. No. ab66746), anti-Rab 7a (Cat. No. ab50533), anti-Lamp 1 (Cat. No. ab25245), anti-cytochrome c (Cat. No. ab133504) antibodies, AF488-conjugated Goat anti-Rabbit (Cat. No. ab150077), AF488-conjugated Goat anti-Mouse (Cat. No. ab150113), AF594-cojugated Goat anti-Rat (Cat. No. ab150160), AF594-cojugated Goat anti-Rabbit (Cat. No. ab150080), and AF488-conjugated Goat anti-Rat (Cat. No. ab150157) secondary antibodies were purchased from Abcam. The anti-fibroblast marker ER-TR7 (Cat. No. sc-73355) antibody was obtained from Santa Cruz. The anti-Caspase 3 (Cat. No. 9662) antibody was obtained from Cell Signaling Technology. The anti-Tubulin (Cat. No. T5168) antibody was purchased from Sigma-Aldrich. The dilution of the antibodies were described in the Supporting Information.

Validation

All antibodies were verified by the supplier and each lot has been quality tested. All validation statements are available on the antibody websites, respectively.

1. Anti-Ki-67: https://www.abcam.com/ki67-antibody-ab15580.html
2. Anti-HMGB1: https://www.abcam.com/hmgb1-antibody-epr3507-ab79823.html
3. Anti-GSDME: https://www.abcam.com/dfna5gsdme-antibody-epr19859-n-terminal-ab215191.html
4. Anti-GSDMD: https://www.abcam.com/gsdmd-antibody-epr19829-ab210070.html
5. Anti-RIP1: https://www.abcam.com/rip-antibody-epr4689-ab125072.html
6. Anti-p-RIP3: https://www.abcam.com/rip3-phospho-s227-antibody-epr9627-ab209384.html
7. Anti-MLKL: https://www.abcam.com/mlkl-antibody-epr17514-ab184718.html
8. Anti-p-MLKL: https://www.abcam.com/mlkl-phospho-s358-antibody-epr9514-ab187091.html
9. Anti-GPX4: https://www.abcam.com/glutathione-peroxidase-4-antibody-epncir144-ab125066.html
10. Anti-PLC-G1: https://www.abcam.com/phospholipase-c-gamma-1plc-gamma-1-antibody-ab107455.html
11. Anti-p-PLC-G1: https://www.abcam.com/phospholipase-c-gamma-1plc-gamma-1-phospho-y783-antibody-ep1898y-ab76031.html
12. Anti-Rab 5a: https://www.abcam.com/rab5-antibody-3a4-early-endosome-marker-ab66746.html
13. Anti-Rab 7a: https://www.abcam.com/rab7-antibody-rab7-117-late-endosome-marker-ab50533.html
14. Anti-Lamp 1: https://www.abcam.com/lamp1-antibody-1d4b-ab25245.html
15. Anti-ER-TR7: https://www.scbt.com/p/fibroblast-marker-antibody-er-tr7;jsessionid=GOOoFFrUI7iAOXWU4JaqEjGedXIVb1fsoIq3IpaDx2qSJnkeputR!-1047972008?productCanUrl=fibroblast-marker-antibody-er-tr7&_requestid=2124072
16. Anti-Caspase 3: https://www.cellsignal.com/products/primary-antibodies/caspase-3-antibody/9662
17. Anti-Tubulin: https://www.sigmaaldrich.com/catalog/product/sigma/t5168?lang=en&region=HK
18. Anti-cytochrome c: https://www.abcam.com/cytochrome-c-antibody-epr1327-ab133504.html
19. AF488-conjugated Goat anti-Rabbit secondary antibody: https://www.abcam.com/goat-rabbit-igg-hl-alexa-fluor-488-ab150077.html
20. AF488-conjugated Goat anti-Mouse secondary antibody: https://www.abcam.com/goat-mouse-igg-hl-alexa-fluor-488-ab150113.html
21. AF594-cojugated Goat anti-Rat secondary antibody: https://www.abcam.com/goat-rat-igg-hl-alexa-fluor-594-ab150160.html
22. AF594-cojugated Goat anti-Rabbit secondary antibody:
23. AF488-conjugated Goat anti-Rat secondary antibody: https://www.abcam.com/goat-rat-igg-hl-alexa-fluor-488-ab150157.html

Eukaryotic cell lines

Policy information about cell lines

Cell line source(s)

A549 lung carcinoma (1101HUM-PUMC000002), MCF-7 (3101HUMSCSP531), MDA-MB-231 (1101HUM-PUMC000014) and 4T1 breast cancers (3101MOUSCSP5056), Hela cervical carcinoma (1101HUM-PUMC000011), SKOV3 ovarian cancer (4201PAT-CCTCC01017), A431 epidermal carcinoma (1101HUM-PUMC000092), HT29 (1101HUM-PUMC000109) and CT26 colon cancer (1101MOU-PUMC000275), human umbilical vein endothelial cells (HUVEC, 4201PAT-CCTCC00692), 3T3/NIH fibroblast cells (1101MOU-PUMC000018) and normal human mammary epithelial cells (MCF-10A, 1101HUM-PUMC000406) were all purchased from National Infrastructure of Cell Line Resource. The human hepatic stellate cell line LX-2 was purchased from Xiangya School of Medicine, Central South University (Hunan, China). The immortalized bone marrow-derived macrophage (iBMDM) was a gift from Dr. Feng Shao of National Institute of Biological Sciences, Beijing. Caspase 3–/–Hela cell was a gift from Dr. Zhengfan Jiang of Peking University, Beijing. HN5 head-neck cancer was a gift from Dr. Jinming Gao of UT Southwestern Medical Center, USA. The mouse alveolar epithelial cell line (AEC) was primary cultured from the lung tissues of fetal mouse.

Authentication

Short tandem repeat (STR) DNA finger printing or morphological features were applied to authenticate and identify cell lines used in this study.

Mycoplasma contamination

All cell lines were tested for mycoplasma contamination. No mycoplasma contamination was found.

Commonly misidentified lines
(See ICLAC register)

No commonly misidentified cell lines are used in this study.

Palaeontology and Archaeology

Specimen provenance

Provide provenance information for specimens and describe permits that were obtained for the work (including the name of the issuing authority, the date of issue, and any identifying information).

Specimen deposition	*Indicate where the specimens have been deposited to permit free access by other researchers.*
Dating methods	*If new dates are provided, describe how they were obtained (e.g. collection, storage, sample pretreatment and measurement), where they were obtained (i.e. lab name), the calibration program and the protocol for quality assurance OR state that no new dates are provided.*

☐ Tick this box to confirm that the raw and calibrated dates are available in the paper or in Supplementary Information.

Ethics oversight	*Identify the organization(s) that approved or provided guidance on the study protocol, OR state that no ethical approval or guidance was required and explain why not.*

Note that full information on the approval of the study protocol must also be provided in the manuscript.

Animals and other organisms

Policy information about studies involving animals; ARRIVE guidelines recommended for reporting animal research

Laboratory animals	Female nu/nu nude mice (6-8 weeks), NOD-SCID mice (6-8 weeks) and BALB/c mice (6-8 weeks) were purchased from Vital River Laboratory Animal Center (China), and kept under specific pathogen free (SPF) condition for one week before the studies, with free access to standard food and water. All care and handling of animals were performed with the approval of the Ethics Committee of Peking University (Protocol number LA2019039). Animals were housed in groups of 4–5 mice per cage, maintained at a temperature of ~25 °C in a humidity-controlled environment with a 12 h light/dark cycle.
Wild animals	No wild animal was used in this study.
Field-collected samples	No field collected samples were involved in this study.
Ethics oversight	All care and handling of animals were performed with the approval of the Ethics Committee of Peking University.

Note that full information on the approval of the study protocol must also be provided in the manuscript.

Human research participants

Policy information about studies involving human research participants

Population characteristics	*Describe the covariate-relevant population characteristics of the human research participants (e.g. age, gender, genotypic information, past and current diagnosis and treatment categories). If you filled out the behavioural & social sciences study design questions and have nothing to add here, write "See above."*
Recruitment	*Describe how participants were recruited. Outline any potential self-selection bias or other biases that may be present and how these are likely to impact results.*
Ethics oversight	*Identify the organization(s) that approved the study protocol.*

Note that full information on the approval of the study protocol must also be provided in the manuscript.

Clinical data

Policy information about clinical studies

All manuscripts should comply with the ICMJE guidelines for publication of clinical research and a completed CONSORT checklist must be included with all submissions.

Clinical trial registration	*Provide the trial registration number from ClinicalTrials.gov or an equivalent agency.*
Study protocol	*Note where the full trial protocol can be accessed OR if not available, explain why.*
Data collection	*Describe the settings and locales of data collection, noting the time periods of recruitment and data collection.*
Outcomes	*Describe how you pre-defined primary and secondary outcome measures and how you assessed these measures.*

Dual use research of concern

Policy information about dual use research of concern

Hazards

Could the accidental, deliberate or reckless misuse of agents or technologies generated in the work, or the application of information presented in the manuscript, pose a threat to:

No	Yes	
☐	☐	Public health
☐	☐	National security
☐	☐	Crops and/or livestock
☐	☐	Ecosystems
☐	☐	Any other significant area

Experiments of concern

Does the work involve any of these experiments of concern:

No	Yes	
☐	☐	Demonstrate how to render a vaccine ineffective
☐	☐	Confer resistance to therapeutically useful antibiotics or antiviral agents
☐	☐	Enhance the virulence of a pathogen or render a nonpathogen virulent
☐	☐	Increase transmissibility of a pathogen
☐	☐	Alter the host range of a pathogen
☐	☐	Enable evasion of diagnostic/detection modalities
☐	☐	Enable the weaponization of a biological agent or toxin
☐	☐	Any other potentially harmful combination of experiments and agents

ChIP-seq

Data deposition

☐ Confirm that both raw and final processed data have been deposited in a public database such as GEO.

☐ Confirm that you have deposited or provided access to graph files (e.g. BED files) for the called peaks.

Data access links *May remain private before publication.*	*For "Initial submission" or "Revised version" documents, provide reviewer access links. For your "Final submission" document, provide a link to the deposited data.*
Files in database submission	*Provide a list of all files available in the database submission.*
Genome browser session (e.g. UCSC)	*Provide a link to an anonymized genome browser session for "Initial submission" and "Revised version" documents only, to enable peer review. Write "no longer applicable" for "Final submission" documents.*

Methodology

Replicates	*Describe the experimental replicates, specifying number, type and replicate agreement.*
Sequencing depth	*Describe the sequencing depth for each experiment, providing the total number of reads, uniquely mapped reads, length of reads and whether they were paired- or single-end.*
Antibodies	*Describe the antibodies used for the ChIP-seq experiments; as applicable, provide supplier name, catalog number, clone name, and lot number.*
Peak calling parameters	*Specify the command line program and parameters used for read mapping and peak calling, including the ChIP, control and index files used.*
Data quality	*Describe the methods used to ensure data quality in full detail, including how many peaks are at FDR 5% and above 5-fold enrichment.*
Software	*Describe the software used to collect and analyze the ChIP-seq data. For custom code that has been deposited into a community repository, provide accession details.*

Flow Cytometry

Plots

Confirm that:

☒ The axis labels state the marker and fluorochrome used (e.g. CD4-FITC).

☒ The axis scales are clearly visible. Include numbers along axes only for bottom left plot of group (a 'group' is an analysis of identical markers).

☒ All plots are contour plots with outliers or pseudocolor plots.

☒ A numerical value for number of cells or percentage (with statistics) is provided.

Methodology

Sample preparation	Cells were trypsinized, harvested and washed with PBS and then analysed with flow cytometer. In some experiments, cells were stained with antibodies or probes according to the manufacturer's protocols, and then analyzed by flow cytometry.
Instrument	Beckman Coulter CytoFlex Flow Cytometer
Software	FlowJo software package (Flowjo V10)
Cell population abundance	Each experiment involved only one type of cell lines and no sorting was performed.
Gating strategy	In general, cells were first gated on FSC/SSC, and single cells were gated using FSC-H and FSC-Width. Cellular uptake, probes and biomarkers were analyzed on the single cell population.

☒ Tick this box to confirm that a figure exemplifying the gating strategy is provided in the Supplementary Information.

Magnetic resonance imaging

Experimental design

Design type	*Indicate task or resting state; event-related or block design.*
Design specifications	*Specify the number of blocks, trials or experimental units per session and/or subject, and specify the length of each trial or block (if trials are blocked) and interval between trials.*
Behavioral performance measures	*State number and/or type of variables recorded (e.g. correct button press, response time) and what statistics were used to establish that the subjects were performing the task as expected (e.g. mean, range, and/or standard deviation across subjects).*

Acquisition

Imaging type(s)	*Specify: functional, structural, diffusion, perfusion.*
Field strength	*Specify in Tesla*
Sequence & imaging parameters	*Specify the pulse sequence type (gradient echo, spin echo, etc.), imaging type (EPI, spiral, etc.), field of view, matrix size, slice thickness, orientation and TE/TR/flip angle.*
Area of acquisition	*State whether a whole brain scan was used OR define the area of acquisition, describing how the region was determined.*

Diffusion MRI ☐ Used ☐ Not used

Preprocessing

Preprocessing software	*Provide detail on software version and revision number and on specific parameters (model/functions, brain extraction, segmentation, smoothing kernel size, etc.).*
Normalization	*If data were normalized/standardized, describe the approach(es): specify linear or non-linear and define image types used for transformation OR indicate that data were not normalized and explain rationale for lack of normalization.*
Normalization template	*Describe the template used for normalization/transformation, specifying subject space or group standardized space (e.g. original Talairach, MNI305, ICBM152) OR indicate that the data were not normalized.*
Noise and artifact removal	*Describe your procedure(s) for artifact and structured noise removal, specifying motion parameters, tissue signals and physiological signals (heart rate, respiration).*
Volume censoring	*Define your software and/or method and criteria for volume censoring, and state the extent of such censoring.*

Statistical modeling & inference

Model type and settings	*Specify type (mass univariate, multivariate, RSA, predictive, etc.) and describe essential details of the model at the first and second levels (e.g. fixed, random or mixed effects; drift or auto-correlation).*
Effect(s) tested	*Define precise effect in terms of the task or stimulus conditions instead of psychological concepts and indicate whether ANOVA or factorial designs were used.*

Specify type of analysis: ☐ Whole brain ☐ ROI-based ☐ Both

Statistic type for inference (See Eklund et al. 2016)	*Specify voxel-wise or cluster-wise and report all relevant parameters for cluster-wise methods.*
Correction	*Describe the type of correction and how it is obtained for multiple comparisons (e.g. FWE, FDR, permutation or Monte Carlo).*

Models & analysis

n/a	Involved in the study	
☐	☐	Functional and/or effective connectivity
☐	☐	Graph analysis
☐	☐	Multivariate modeling or predictive analysis

Functional and/or effective connectivity	*Report the measures of dependence used and the model details (e.g. Pearson correlation, partial correlation, mutual information).*
Graph analysis	*Report the dependent variable and connectivity measure, specifying weighted graph or binarized graph, subject- or group-level, and the global and/or node summaries used (e.g. clustering coefficient, efficiency, etc.).*
Multivariate modeling and predictive analysis	*Specify independent variables, features extraction and dimension reduction, model, training and evaluation metrics.*